Atmos. Chem. Phys. Discuss., 8, 11685–11754, 2008
www.atmos-chem-phys-discuss.net/8/11685/2008/

Atmospheric Chemistry and Physics Discussions

Gas phase precursors to anthropogenic secondary organic aerosol: detailed observations of 1,3,5-trimethylbenzene photooxidation

K. P. Wyche[1], P. S. Monks[1], A. M. Ellis[1], R. L. Cordell[1], A. E. Parker[1], C. Whyte[1], A. Metzger[2], J. Dommen[2], J. Duplissy[2], A. S. H. Prevot[2], U. Baltensperger[2], A. R. Rickard[3], and F. Wulfert[4]

[1]Atmospheric Chemistry, Dept. of Chemistry, Univ. of Leicester, Leicester, LE1 7RH, UK
[2]Laboratory of Atmospheric Chemistry, Paul Scherrer Institut, 5232, Villigen, Switzerland
[3]National Centre for Atmospheric Science, University of Leeds, Leeds, LS2 9JT, UK
[4]Division of Food Sciences, University of Nottingham, Sutton Bonington Campus, Loughborough, LE12 5RD, UK

Received: 15 April 2008 – Accepted: 13 May 2008 – Published: 13 June 2008

Correspondence to: P. S. Monks (p.s.monks@le.ac.uk)

Published by Copernicus Publications on behalf of the European Geosciences Union.

Abstract

A series of photooxidation experiments were conducted in an atmospheric simulation chamber in order to investigate the secondary organic aerosol (SOA) formed from the anthropogenic model gas phase precursor, 1,3,5-trimethylbenzene. Alongside specific aerosol measurements, comprehensive gas phase measurements, primarily by chemical ionisation reaction time-of-flight mass spectrometry (CIR-TOF-MS), were carried out to provide detailed insight into the composition and behaviour of the organic components of the gas phase matrix during SOA formation. An array of gas phase organic compounds was measured during the oxidation process, including several previously unmeasured primary bicyclic compounds possessing various functional groups. Analysis of results obtained during this study implies that these peroxide bicyclic species along with a series of furanones and organic acids contribute to SOA growth. The effect of varying the VOC/NO_x ratio on SOA formation was explored, as was the effect of acid seeding. It was found that low NO_x conditions favour more rapid aerosol formation and a higher aerosol yield, a finding that points towards a role for organic peroxides in the nucleation process and SOA growth.

1 Introduction

Secondary organic aerosol (SOA) is formed in the atmosphere from the oxidation products of certain biogenic and anthropogenic volatile organic compounds (VOCs) (Finlayson-Pitts and Pitts Jr., 2000). One important class of such compounds known to be precursors to SOA are aromatic hydrocarbons (Stern et al., 1987; Odum et al., 1997). Possessing complex and extensive atmospheric reaction pathways, aromatic VOCs (AVOCs) have the ability to yield a wide array of secondary oxygenated and nitrated volatile, semi-volatile and non-volatile organic products which contain a multitude of different functional groups (e.g. Atkinson, 2000; Hamilton et al., 2003; Johnson et al., 2005; Sax et al., 2005; Bloss et al., 2005b).

Released principally from automobile exhaust emissions, industrial scale combustion and the evaporation of fuels and solvents (Friedrich and Obermeier, 1999), AVOCs make up as much as 40% of the total mass of anthropogenic hydrocarbon emissions in the city environment (Smith et al., 1999). On the global scale total aromatic emissions are of the order 15.8 $Tg\,y^{-1}$ (Tsigaridis and Kanakidou, 2003), which account for ∼15% of the annual anthropogenic non-methane hydrocarbon (NMHC) budget (Bloss et al., 2005a). As well as constituting precursors to SOA production, AVOCs generally have high photochemical ozone creation potentials and hence contribute significantly towards tropospheric ozone pollution (Calvert et al., 2002; Derwent et al., 2003; Derwent et al., 2007a; Derwent et al., 2007b).

It has been established that SOA mass constitutes a major fraction of the total atmospheric loading of organic aerosol and indeed the more general class of atmospheric particulate matter, on both the local (Baltensperger et al., 2005) and the global (Kanakidou et al., 2005) scale. Under certain scenarios atmospheric SOA can comprise as much as 90% of organic aerosol mass (Kalberer et al., 2004) and 50% of the total mass of atmospheric aerosol (Kleindienst et al., 1999).

The existence of SOA in the atmosphere (and particulate matter in general) has an array of well documented consequences (e.g. Czoschke et al., 2003; Kanakidou et al., 2005; IPCC, 2007 and references therein). In brief, such negative effects range from visibility impairment on the local scale to climate change, with SOA being capable of perturbing the Earth's radiative budget via both direct and indirect mechanisms. Additionally, fine airborne particles have been shown to exert numerous detrimental effects on human health, particularly in vulnerable members of the population (Grosjean, 1992).

As highlighted in recent reviews (e.g. Seinfeld and Pankow, 2003; Kanakidou et al., 2005; Holmes, 2007), despite its crucial role in the Earth-atmosphere system, there currently remains a certain lack of understanding regarding the physical and chemical properties of SOA, its chemical composition and crucially the atmospheric processes by which it is formed.

Over the last decade much research and many state-of-the-art techniques have been applied to the critical problem of determining SOA chemical composition, with off-line GC-MS analysis of filter samples often providing the foundation. However, such studies have supplied limited molecular level classification, with generally no more than 30% of the total SOA mass being identified (e.g. Forstner et al., 1997; Kleindienst et al., 1999; Cocker III et al., 2001; Hamilton et al., 2003; Edney et al., 2005; Surratt et al., 2006).

A series of recent discoveries have allowed significant advancement in our understanding of SOA composition and the role of low molecular mass species in aerosol growth. It has been proposed that between 20 and 50% of SOA mass could be comprised of large multi-functional macromolecular compounds known as "humic-like substances" (HULIS) (Havers et al., 1998), which would go undetected using standard GC-MS techniques. Research has suggested that such compounds are secondary in nature, being formed by heterogeneous polymerisation/oligomerisation reactions in the aerosol. For example, Jang and Kamens (Jang and Kamens, 2001) witnessed an increase in SOA yield when various gas phase aldehydic species were injected into a synthetic air matrix impregnated with acidic seed particles. The authors attribute the increase in SOA mass to heterogeneous hydration and polymerisation reactions of low molecular mass aldehydes following their transfer from the gas phase. Their findings also indicated that hemiacetal/acetal formation is also an important contributing pathway to increased SOA yields when alcohols were also present.

Numerous investigations have since confirmed the existence of polymeric/oligomeric compounds in various SOA systems of both anthropogenic (Gross et al., 2006) and biogenic (Surratt et al., 2006) origin, both in simulation chamber studies (Baltensperger et al., 2005) and in the "real" atmosphere (Kalberer et al., 2006), with molecular masses as large as 1600 Da (Gao et al., 2004). One such study by Kalberer et al. demonstrated that as much as 50% of the SOA mass formed during the photooxidation of 1,3,5-trimethylbenzene was composed of polymers (Kalberer et al., 2004). The authors proposed that the polymers, which were detected with masses as high as 1000 Da, were formed primarily through acetal polymerisation involving the known trimethylbenzene

photooxidation product methyl glyoxal in the presence of water.

With a large portion of current research into SOA formation geared towards investigation of the aerosol phase, there exists a distinct lack of detailed understanding of the concomitant gas phase organic components of the system. Limited work has also been conducted in elucidating the actual mechanisms of SOA formation. Recently, research has shown that the SOA forming capacity of aromatic systems is strongly related to [NO_x], with greater SOA yields obtained under low NO_x conditions (Izumi et al., 1988; Stroud et al., 2004; Song et al., 2005; Ng et al., 2007). Conclusions from such work have inferred an important role for gas phase organic peroxides in initiating the formation of SOA (Johnson et al., 2004), but no direct evidence is available to support this.

In the present study we begin to address these issues by presenting findings from a series of comprehensive photooxidation experiments in an atmospheric simulation chamber. The main aim of the study was to monitor, in detail and with good temporal resolution, the complex array of organic gas phase oxidation products derived from a known SOA precursor and to identify potential species contributing to incipient aerosol formation and growth. In this instance the common, but less well studied anthropogenic AVOC, 1,3,5-trimethylbenzene (TMB), was chosen as a model anthropogenic SOA precursor. The effect of variation of the initial VOC/NO_x ratio on SOA formation was also explored, as was the role of potential acid-catalysed heterogeneous chemistry. As well as presenting information that provides new insight into the mechanisms of SOA forming intermediates and potential SOA forming species, this work presents the first measurements of a set of previously undetected high mass oxygen-bridged bicyclic compounds, which are formed during aromatic oxidation.

In a companion article[1] (here after referred to as Rickard et al., 2008) the gas phase measurements presented here are compared with the output of a box model employing

[1]Rickard, A. R., Wyche, K. P., Metzger, A., Monks, P. S., Ellis A. M., and Pilling, M. J.: Model-measurement comparisons of the evolution of the gas-phase precursors to secondary organic aerosol formed in the photooxidation of 1,3,5-trimethylbenzene, in preparation, 2008.

data extracted from the Master Chemical Mechanism (MCMv3.1; http://mcm.leeds.ac.uk/MCM). The findings of this complementary study support the results obtained here and in combination they provide further insight into the identity of potential SOA forming species.

2 Experimental

2.1 The Paul Scherrer Institut aerosol chamber

Experiments were carried out at the aerosol chamber facility at the Paul Scherrer Institut. The chamber comprises a single-lined collapsible bag constructed from DuPont Teflon fluorocarbon film, with a wall thickness of 125 μm and a volume of 27 m^3 ($3\times3\times3\,m^3$). The chamber surface area to volume ratio ($2\,m^{-1}$) is relatively small when compared to most environment chambers, allowing wall effects to be minimized. The chamber bag is held by a large metal frame inside a temperature-controlled wooden housing, which was maintained at 20°C (±1°C) during all experiments. Four 4 kW xenon arc lamps, deployed at various points inside the housing, are employed to simulate the solar spectrum (Paulsen et al., 2005).

The chamber sample gas comprised purified ambient air, which was produced by a clean air generator (AADCO Instruments Inc., USA). Chamber humidification was facilitated by bubbling the bulk matrix gas through a heated glass vessel containing high purity deionized water (15 MΩ) prior to the injection of other compounds. The chamber humidity was typically near 50% during each experiment.

Delivery of the VOC SOA precursor to the chamber took place via syringe injection of the liquid compound into a heated injector port, which facilitated compound volatilisation before entry into the bag. A period of 30 min was allowed for mixing to create a homogeneous sample matrix before any measurements were made.

In order to remove any potential organic impurities from the chamber and hence to eliminate unwanted artefacts from the data (in the form of SOA formed from species

other than the TMB), the chamber bag was scrubbed with ozone (2–7 ppmV) for 5 h, before being flushed thoroughly with purified ambient air for approximately 30 hours prior to each experiment.

On-line measurements of chamber nitric oxide (NO) and NO_x concentrations were made throughout each experiment using a Monitor Labs 9841A NO_x analyser (for NO_x concentrations: 50–2000 ppbV) and a Thermo Environmental Instruments 42C trace level NO_x photolytic converter (for NO_x concentrations: 0–200 ppbV). Ozone measurements were also conducted in real-time using an ozone analyser (Environics model S300). The aerosol phase was monitored using two TSI (3025 and 3022A) condensation particle counters (CPC, size range: particle diameter (D_p) $\geq$3 nm) and a Sampling Mobility Particle Sizer (SMPS, size range: $15 \leq D_p \leq 690$ nm), providing information on the total number density of particles in the chamber along with particle geometric mean diameter and aerosol volume concentration (see Dommen et al., 2006 for further instrument details).

2.2 Experiment design

In order to explore the effect of NO_x on the TMB-SOA system, experiments were conducted with various initial VOC/NO_x ratios. For the first part of the study, chamber experiments were conducted with high concentrations of VOC (>500 ppbV) and NO_x (>250 ppbV). For these high NO_x experiments nitric oxide and nitrogen dioxide (NO_2) gases (Air Liquide, Ch., grade N6.0) were added to the chamber via an inlet injection system prior to introduction of the VOC. Experiments with initial VOC/NO_x ratios of approximately 2:1, 2:1 (with NO only) and 1:2 were carried out during the high NO_x part of the study.

As well as conducting "high" concentration chamber experiments with input of all gases before initiation of the photochemistry, two "low" concentration experiments were conducted in order to simulate more realistic atmospheric conditions. In these experiments a constant low level source of nitrous acid (HONO) was used to supply NO to the system in place of NO and NO_2 gases. HONO was produced by reaction of a

sodium nitrite solution with sulfuric acid in a flow system. A nitrogen carrier gas was passed through the mixture continuously in order to purge nitrous acid vapour out and into the chamber bag (Taira and Yukio, 1990). This process provided a constant HONO mixing ratio of roughly 10 ppbV throughout the experiment. Consequently, the low concentration experiments had high initial VOC/NO_x ratios of ~16:1. In order to provide a brief exploration into the effect of an inorganic seed, for Experiment 7, 400 pptV sulphur dioxide (SO_2) gas was added to the chamber. Table 1 lists the specific starting conditions used for each experiment.

2.3 VOC/OVOC measurement with chemical ionisation reaction time-of-flight mass spectrometry

The gas phase organic compounds within the chamber were monitored using a newly developed chemical ionisation reaction time-of-flight mass spectrometer (CIR-TOF-MS). TOF-MS comes into its own when dealing with such complex mixtures since the entire spectrum is captured in any one instant. Furthermore, the technique is not constrained by upper mass limits and its standard resolution is usually far higher than more conventional quadrupole mass spectrometers. Therefore, important advantages of CIR-TOF-MS in this instance include the ability to detect a comprehensive set of organic compounds, including oxygenated VOCs (OVOCs) and species of quite high molecular masses and the ability to assist compound identification on the basis of accurate mass measurements. Details regarding the instrument and its performance have been given previously (Blake et al., 2003; Wyche et al., 2007), and hence only a brief and experiment-specific review is provided here.

The CIR-TOF-MS comprises a radioactive ion source/drift cell assembly, coupled to an orthogonal time-of-flight mass spectrometer equipped with a wide bore reflectron array. In the current study proton transfer was used as the means of ionization and the proton donor was the hydronium ion (H_3O^+) (Lindinger et al., 1993). In order to generate the primary reagent ions, water vapour was delivered to the ion source by bubbling a high purity nitrogen carrier gas (Air Liquid, Ch, grade 7.0) through a

glass vessel containing ultra-pure deionized water (15 MΩ) at a rate of 30–52 sccm. Sample air from the PSI aerosol chamber was delivered to the CIR-TOF-MS at a rate of 200–275 sccm via an insulated 2 m long Teflon line and a PTFE critical orifice. Both the sample line and critical orifice were heated to 40°C (±1°C) in order to limit wall losses. For brief intervals during certain experiments a particle filter was placed in the sample line to verify that all measured signals were due to gas phase species. The combined reagent and sample gas flows led to drift cell operating pressures in the range 6–9 mbar. A positive potential difference was applied across the drift cell to guide the ions into the mass spectrometer. The drift cell electric field (and therefore internal energy) was varied for certain experiments in order to enhance sensitivity to certain VOCs. The potential difference between the final two electrodes of the cell was varied to facilitate collision-induced dissociation of the ionised sample and hence to allow controlled removal of unwanted water cluster ions, i.e. $MH^+.(H_2O)_n$ (where M represents the target VOC). The experiment specific drift cell E/N ratios (where E is the electric field and N is the gas number density) are provided in Table 1.

As stated earlier, an important feature of time-of-flight mass spectrometry is the ability to achieve a much higher mass resolution than alternative techniques, noticeably quadrupole mass spectrometry. The mass resolution attained in the current study was in the region of 0.01 Da and this has proved useful in confirming the assignment of several high mass peaks.

The sum of hydro and organic peroxy radicals (i.e. $\sum(HO_2+\Sigma_i R_i O_2)$) present in the chamber was also measured during low NO_x experiments using a dual channel Peroxy Radical Chemical Amplifier (PERCA). The PERCA deployed during this work was similar to that described in Green et al., 2006, but with inlet systems as per Monks et al., 1998.

2.4 Calibration issues

A wide array of compounds was detected using the CIR-TOF-MS and it was therefore impractical to carry out independent calibrations for all measured species. Consequently, where no calibration standard was available for a given compound the calibration factor determined for a structurally similar surrogate was utilised. If no appropriate surrogate could be found, measurements are reported in terms of instrument signal (i.e. normalised ion counts per second (ncps) see Sect. 3.7). VOC yields quoted in the following discussion therefore act only as a guide for those compounds where surrogates have been employed. Table A1 in the supporting information provides comprehensive details of all VOC calibrations employed in the current study. Considering all instrument and calibration associated uncertainties (Wyche et al., 2007), the overall CIR-TOF-MS measurement errors lay within the range 2.9–27.6% (see Table A1).

Owing to experimental time constraints, a PERCA chain length calibration was not carried out following all experiments. Consequently, a typical chain length of 109 (obtained from previous experiments; Parker, 2007) was assumed to provide reasonable estimates of the peroxy radical concentrations. The amplification chain length of the PERCA varies between ~80 and 150. When combined with instrument uncertainties this gives an estimated peroxy radical uncertainty of 42% (Fleming et al., 2006a; Fleming et al., 2006b).

3 Results and discussion

The chamber conditions in this work can be broadly divided into two groups, high NO_x and low NO_x. In the high NO_x experiments the initial NO_x concentration was >250 ppbV, whereas low NO_x conditions corresponded to NO_x at ≤5 ppbV. The results from the high and low NO_x experiments are reported separately in the following sections. Comparisons of gas and aerosol phase measurements carried out under different VOC/NO_x regimes are utilised during the present study to help elucidate the underlying SOA formation mechanisms.

3.1 Chamber inorganic species and the SOA precursor under high NO_x conditions

The majority of experiments (Experiments 1–4 and 6; see Table 1) were carried out under high NO_x conditions. During these experiments the initial VOC/NO_x ratio was varied between 0.54 and 2.25.

Figure 1a–d displays the temporal evolution of the major inorganic gas phase components of the chamber system and the 1,3,5-trimethylbenzene precursor in several different experiments. In all instances the experiment start time is taken from the point at which chamber lights were switched on and hence the photochemistry initiated. On average the duration of each experiment was of the order of 9–10 h.

Figure 1a summarises the findings for Experiment 6. Experiment 6 constitutes a typical example of a high NO_x Experiment with VOC/NO_x~2:1; hence it is used as focus for discussion. The Experiment essentially begins with the production of ground state atomic oxygen, which originates from the photolysis of NO_2. This results in the subsequent production of ozone, photolysis of which in the presence of water, yields OH. OH can also be generated in such systems from HONO photolysis, which is generally produced in all chamber systems following wall reactions involving NO_2 (e.g. Metzger et al., 2008a[2]). Following its generation, OH reacts with TMB to subsequently generate a complex array of oxidation products, including organic peroxy radicals (RO_2), hydroperoxy radicals (HO_2) and oxygenated and nitrated VOCs (Calvert et al., 2002).

The oxidation profiles for TMB during all high NO_x experiments exhibited similar behaviour, with a short initial concentration plateau corresponding to the time required to initiate the OH chemistry, followed by a peak in oxidation rate ~160 min after lights on. After this period, the TMB concentration profile was characterised by a roughly constant decay. For each high NO_x experiment a plot of ln[TMB] vs. time is approx-

[2]Metzger, A., Dommen, J., Gaeggeler, K., Duplissy, J., Prevot, A. S. H., Kleffmann, J., Elshorbany, Y., Wisthaler, A., and Baltensperger, U.: Evaluation of 1,3,5-trimethylbenzene degredation in the detailed tropospheric chemistry mechanism MCMv3.1 using environmental chamber data, in preparation, 2008a.

imately linear, with no distinct change in rate with accumulation of ozone. Consequently with NO_3 oxidation of TMB negligible under the experimental chamber conditions used, the major chemical loss of TMB results solely from its reaction with OH. An estimation of [OH] can therefore be inferred from the TMB decay recorded by CIR-TOF-MS. For experiments with an initial VOC/NO_x ratio of ~2:1, peak OH concentrations were ~0.04 pptV and experiment average concentrations were ~0.03 pptV (using $k_{OH+1,3,5TMB}=(5.67\pm1.13)\times10^{-11}$ cm^3 molecules^{-1} s^{-1} at $T=298$ K Calvert et al., 2002).

With the production of both HO_2 and RO_2 radicals, NO became oxidised to NO_2, leading to the concentration peak seen in Fig. 1a–c. Due to the presence of the VOC (and hence RO_2), the NO/NO_2 partitioning was such that there was a positive deviation from the photostationary state resulting in net initial ozone production (Monks, 2005). As noted in other chamber studies (e.g. Bloss et al., 2005a; Dommen et al., 2006), the peak in [NO_2] and the initial accumulation of O_3 roughly coincide with the observed maximum rate of loss of the VOC and the peak in [OH]. Eventually, NO_2 is removed from the gas phase through the production of nitric acid (HNO_3) via reactions on the chamber walls and incorporation into organic nitrates and the aerosol phase (Monks, 2005). As NO_2 chemistry constitutes the sole route to O_3 formation within the chamber, the removal of NO_x from the system was followed by a fall in the concentration of O_3. At the conclusion of Experiment 6, ~70% of the VOC precursor had been consumed and the concentrations of NO and NO_2 had fallen to negligible levels (Fig. 1a). For Experiment 2 (VOC/NO_x~2:1) shown in Fig. 1b, initial NO_x was introduced solely in the form of NO and starting concentrations were set to two times those of other high NO_x experiments with VOC/NO_x~2:1. To initiate the oxidation process in this instance, HONO and NO_2had first to be liberated from the illuminated chamber walls following known heterogeneous chemical mechanisms (Stroud et al., 2004; Metzger et al., 2008a[2]).

Experiment 3 involved a reversal of the VOC/NO_x ratio to a value of roughly 1:2, but still with high starting concentrations. As can be seen in Fig. 1c the NO_x, O_3 and TMB components of the system exhibited similar profiles to those observed during the other high NO_x experiments, but with a number of key exceptions. When the VOC/NO_x ratio

was decreased to ∼0.5, the rate of decay of TMB appeared enhanced, suggesting higher levels of oxidant. In this instance inferred OH radical levels were on average ∼0.06 pptV, i.e. twice as high as levels observed in the other high NO_x experiments. This is likely to result from balancing of the OH/HO_2 ratio in the hydroxyl radical cycle, where a relatively higher proportion of NO (with respect to that of the VOC) will force a shift towards OH in the chamber HO_x balance. The impact of an elevated OH density is reflected in the amount of VOC consumed by the conclusion of the experiment, i.e. after 600 min less than 10% of the initial TMB remained. In addition to this, a lower RO_2/NO_x ratio will slow the cycling of NO to NO_2 and hence delay subsequent O_3 production. This effect is observed in the data, where a significant delay was indeed observed in the times at which NO_2 and O_3 reached their respective peaks, and at which NO reached negligible concentrations when compared to experiments with VOC/NO_x ∼2:1.

3.2 Chamber inorganic species and the SOA precursor under low NO_x conditions

The second component of the chamber study comprised two low NO_x experiments, Experiments 5 and 7, during which [NO_x] was kept below ∼5 ppbV. In the case of Experiment 7, SO_2 gas was added to the chamber in order to generate sulphuric acid (H_2SO_4) seed particles.

As discussed in Sect. 2.2, during the low NO_x experiments the chamber was supplied with a continuous source of NO (from HONO) at a rate greater than the sum of its removal pathways. Consequently, the chamber remained in a state of net ozone production throughout the experiment and therefore no distinct peak and fall is observed in the ozone concentration profile.

In addition to supplying the chamber with NO, HONO photolysis constituted an additional source of OH. The photolysis rate of nitrous acid (j(HONO)) for the PSI chamber has been measured as $2.7\times10^{-4}\,s^{-1}$, which yields an OH production rate (P(OH)) of $2.7\,pptV\,s^{-1}$ for a constant HONO value of 10 ppbV. As P(OH) from the photolysis of HONO was several times larger than P(OH) from ozone at any instant during the low NO_x experiments, the level of OH in the chamber was roughly constant. Evidence

for this can be seen in Fig. 1d, where the rate of decay of TMB during Experiment 7 remained roughly constant during the majority of the experiment. Using the rate of oxidation of TMB (as described in Sect. 3.1), the average OH concentrations in the chamber for the two low NO_x experiments 5 and 7 were estimated to be ∼0.05 and 0.06 pptV. Tables 1, 2 and 3 lists key measured parameters describing the evolution of the inorganic species for each experiment.

3.3 Chamber aerosol formation under high NO_x conditions

Figure 2a–d summarise the key aerosol phase parameters for the four variants of the TMB photooxidation study, i.e. the total aerosol number density, total aerosol volume and mean geometric particle diameter.

For Experiments 1–6 no seeding was employed in the simulation chamber and hence new aerosol formation occurred via homogeneous nucleation involving certain key semi-and non-volatile oxidation products of the precursor VOC (Seinfeld and Pankow, 2003; Holmes, 2007). The nucleation event observed during Experiment 6 (high NO_x experiment, VOC/NO_x∼2:1) is clearly evident in Fig. 2a, and is seen as a dramatic increase in the total number density of particles in the chamber at ∼185 min. In this study we define nucleation to have occurred once the differential of the particle number density (with respect to time) exceeds a value of one for 3 consecutive measurements (i.e. when the particle count tends away from the baseline). Nucleation times are given for the CPC and the SMPS instruments in Table 1. However as the CPC measures particles closer in size to the nucleating cluster (i.e. ∼1.5 nm), those values are employed during the following analysis and discussion.

In Experiment 6 new SOA formation continued for some 100 min, by which time a maximum number density of ∼490 particles cm^{-3} was reached (in the size range 15–690 nm). During this time, via condensation and then coagulation mechanisms, the particles grew in size to a maximum mean diameter of ∼480 nm at ∼490 min. The total volume of chamber SOA followed a similar trend to that of particle diameter. Ultimately the number density of SOA particles and the total suspended chamber mass

decreased owing to coagulation and deposition to the chamber walls. Table 2 highlights the reproducibility of aerosol phase parameters between repeat studies of the three high NO_x experiments carried out at VOC/NO_x~2:1 (Experiments 1, 4 and 6).

Following the analysis performed in Baltensperger et al., 2005, total SOA mass has been determined from the measured SOA volume by assuming a density of 1.4 g cm^{-3}. In the case of Experiment 6, a maximum SOA mass of 31 μg m^{-3} was reached. As no wall loss corrections have been applied to the aerosol phase data, this value constitutes a lower limit and should be treated with care. Consequently, a "relative" SOA yield (Y) was calculated according to Eq. 1 (after Odum et al., 1996):

$$Y = (M_0/\Delta\text{VOC}) \times 100 \quad (1)$$

In the above expression M_0 corresponds to the peak mass of SOA produced and ΔVOC is the amount of the precursor VOC consumed at the peak SOA mass (both expressed in units of μg m^{-3}). Yields for the three repeat experiments with a VOC/NO_x ratio ~2:1 (i.e. Experiments 1, 4 and 6) were 1.9, 2.3 and 1.8%, respectively.

The temporal behaviour of the measured aerosol parameters for Experiment 2 (VOC/NO_x~2:1, NO only) was similar to those of Experiments 1, 4 and 6. However, as the initial concentration of both TMB and NO was set to twice that of the other high NO_x (VOC/NO_x~2:1) experiments, an approximate two-fold increase in the maximum number density of particles was observed (~1200 particles cm^{-3}). Also, particles grew to possess larger maximum mean diameters (~660 nm) and the ultimate experiment SOA yield was roughly four times greater than that of the other high NO_x experiments (1, 4 and 6), at 7.5%. The findings described here for an enhanced level of starting material are consistent with those previously reported (e.g. Paulsen et al., 2005; Song et al., 2005; Gross et al., 2006).

When the starting VOC/NO_x ratio was reversed to ~1:2 for Experiment 3, SOA formation was significantly delayed, with nucleation occurring around 215 min later than in Experiment 6. By the conclusion of Experiment 3 (~600 min) the chamber aerosol appeared to still be in a state of growth and no distinct peak in either size or mass had

been reached. Consequently, the SOA yield was determined from the aerosol mass produced at the conclusion of the experiment. With a VOC/NO_x ratio of ~1:2, a SOA yield of 0.3% was achieved, i.e. roughly an order of magnitude lower than for the larger VOC/NO_x ratios. With more than 90% of the precursor VOC consumed by termination of the experiment and with primary and secondary oxidation products having reached their concentration peaks, it may be assumed that further aerosol growth after this point would be minimal.

From the above discussion and from inspection of Table 2 it is clear that for each experiment conducted under high NO_x conditions a significant delay or "incubation" period was witnessed before the nucleation event. For Experiments 1, 2, 4 and 6 (VOC/NO_x~2:1) this period lasted for approximately 110, 145, 190 and 185 min, respectively, and for Experiment 3 (VOC/NO_x~1:2) was over twice as long at 400 min. Evidence for this incubation period has been reported for several other aromatic oxidation systems, including benzene, toluene, *o*-xylene and *m*-xylene in a number of different simulation chambers (Izumi et al., 1988; Johnson et al., 2004; Johnson et al., 2005; Song et al., 2005; Ng et al., 2007).

It has been proposed that the existence and duration of the incubation period is directly related to the presence of NO in the gas phase (Johnson et al., 2004; Johnson et al., 2005). Results obtained by Johnson et al. (2005) from a gas phase oxidation model coupled to an absorptive aerosol transfer scheme showed that the less volatile hydroperoxides, formed from the self-reactions of hydro and organic peroxy radical species (R3 and R4), were significant contributors to SOA mass. Consequently, new particle formation and growth could be closely linked to the ambient levels of NO, which may preferentially react with HO_2 and RO_2 via reactions R1 and R2 in the scheme below, limiting the capacity of the system to form peroxides:

$$NO + HO_2 \rightarrow NO_2 + OH \quad (R1)$$

$$NO + RO_2 \rightarrow NO_2 + RO \quad (R2)$$

$$RO_2 + RO_2 \rightarrow ROOR + O_2 \quad (R3)$$

$$RO_2 + HO_2 \rightarrow ROOH + O_2 \quad \text{(R4)}$$

Johnson and co-workers (Johnson et al., 2005) proposed that once in the aerosol phase, the peroxides can take part in heterogeneous chemistry with certain aldehydic species to form peroxyhemiacetals. This thesis supports results from previous studies of various workers demonstrating the importance of heterogeneous chemistry in the aerosol, and in particular acetal and hemiacetal reactions involving carbonyl oxidation products (Jang and Kamens, 2001; Jang et al., 2003).

Through an examination of the kinetics involved with reactions R1–R4, it is possible to infer the influence of the NO concentration on gas phase hydroperoxide formation during the experiments presented here. Equation 2 below accounts for reactions R1–R4 to determine the fraction of RO_2 (Φ) that forms hydroperoxides:

$$\Phi = \{k_4[RO_2][HO_2]\}/\{k_4[RO_2][HO_2] + k_3[RO_2]^2 + k_2[RO_2][NO]\} \quad (2)$$

Figure 3a shows the variation of Φ with NO concentration taken from Experiment 6, for a series of HO_2 and RO_2 concentrations generated from the chamber box model employed in a companion paper (Rickard et al., 2008). Figure 3a clearly demonstrates that for the self-reaction route involving both hydro and organic peroxy radical species to become significant, either high radical levels are required (i.e. tens of pptV) or the concentration of NO must approach zero. For Φ (i.e. hence peroxide formation) to reach as much as 5% in this model, the concentration of NO must fall below 2 ppbV (with ~34 and 51 pptV HO_2 and RO_2, respectively) and for 10%, ~1 ppbV (with ~41 and 61 pptV HO_2 and RO_2, respectively). Comparable results have been obtained here using a chamber box model to generate radical profiles (not shown), employing a mode similar to that used by Ng et al. during chamber studies involving benzene, toluene and *m*-xylene (Ng et al., 2007).

During Experiments 1, 2, 4 and 6 (VOC/NO_x~2:1), the time required for the NO concentration in the chamber to reach 2 ppbV (i.e. to approach zero) ranged from ~150 to 170 min (see Table 2). Contrasting these times with those of the nucleation event

in each case, we see that SOA formation occurs only as [NO] drops towards zero, adding support to the thesis that peroxide chemistry is involved in SOA formation. However, during experiments 4 and 6 there is a further time delay (of ~30 and 20 min, respectively) before particle formation occurs, implications of which are discussed in Sect. 3.5. The concentrations of NO at nucleation for the high NO_x Experiments 1, 2, 4 and 6 were 16.2, 6.2, 1.2, and 1.4 ppbV, respectively. Particle growth during Experiment 1 was slower than other repeat experiments, an observation in line with slightly higher [NO] at the point of SOA formation.

The hypothesis suggesting that the NO concentration in the chamber must reach a minimal value before nucleation can occur is supported by results obtained from varying the VOC/NO_x ratio. When the VOC/NO_x ratio was changed from 2:1 to a nominal value of 1:2 (Experiment 3), a considerably longer time was required for the system chemistry to reduce [NO] to negligible levels (see Table 2). Correspondingly, a delay was observed in the timing of the nucleation event. In addition to this, nucleation did not occur until roughly a further 75 min after [NO] had reached minimal levels.

3.4 Chamber aerosol formation and peroxy radicals under low NO_x conditions

Figure 2 and Table 2 demonstrate the clear difference between the nucleation times of the high and low NO_x experiments. During the low NO_x experiments a distinctly shorter incubation period was observed before the onset of aerosol formation, i.e. ~50 and 20 min for Experiments 5 and 7, respectively, compared to an average of ~155 min for the typical high NO_x experiments (see Fig. 2d). During the low NO_x (constant HONO) experiments the concentration of NO up to the point of nucleation was no greater than ~1 ppbV and an additional radical source was present to supply OH and (therefore HO_2) to the matrix. Consequently, it is highly likely that radical-radical self-reaction routes (R3 and R4) dominated the fate of the RO_2 species from the start of the experiment. It should be noted that the length of the incubation period of each low NO_x experiment (i.e. 5 and 7), is comparable to the length of the time delay between NO falling to negligible concentrations and nucleation during high NO_x Experiments 4

and 6.

The SOA yields obtained during low NO_x Experiments 5 and 7 were 7.9 and 6.2% respectively, i.e. roughly 3.5 and 24.3 times larger than those achieved under high NO_x conditions of VOC/NO_x~2:1 and 1:2, respectively. It should be noted that in the latter instance (Experiment 3, VOC/NO_x~1:2), the experiment was conducted with the same initial TMB concentration as the low NO_x experiments, and thus it is unlikely that enhanced yields under low NO_x conditions are an artefact of initial precursor concentration (Ng et al., 2007). Ng et al. (2007) saw roughly 2.8 and 5.7 fold increases in SOA yields in the toluene and *m*-xylene systems, respectively, when moving from high to low NO_x conditions, comparable to observations made here.

As discussed earlier, recent reports attribute the production of a greater aerosol yield in low NO_x systems to chamber conditions favouring formation of the low volatility peroxides from reactions R3 and R4 (Stern et al., 1987; Jenkin et al., 2003; Johnson et al., 2004; Song et al., 2005; Ng et al., 2007). However, as discussed below the conditions of low NO_x Experiments 5 and 7 also allow an early production of a variety of other organic oxidation products which may further contribute to the enhancement of SOA yield.

Elevated NO_x concentrations, such as those employed during the high NO_x experiments of this study, lead to interference problems in the inlet chain length chemistry when measuring peroxy radical species using the PERCA technique (Green et al., 2006; Parker, 2007). Consequently, peroxy radical data are presented only for experiments conducted under low NO_x conditions. Figure 4 displays the temporal evolution of the sum of both hydro and organic peroxy radicals during Experiment 5, during which a rapid rise in peroxy radical concentration was observed from lights on to a concentration plateau of ~175 pptV by ~400 min. The onset of plateau behaviour in radical concentration was coincident with removal of the precursor VOC from the system, i.e. at plateau ~80% of the TMB had been consumed.

The temporal behaviour of the peroxy radicals during the low NO_x experiments can be attributed to the constant input of OH and NO throughout the experiment and the

subsequent evolution of chamber ozone. As the precursor VOC constitutes the sole source of RO_2, its consumption as the experiment evolves accounts for the observed decrease in rate of peroxy radical production.

Using the partitioning theory outlined in Sect. 3.3 (Eq. 2) along with total peroxy radical and NO measurements, it is possible to demonstrate how peroxide production may proceed within the chamber under low NO_x conditions. Figure 3b shows the variation of Φ with [RO_2] and [NO] using measured data (assuming a typical urban air [HO_2]/[RO_2] ratio of 2:3). With the NO concentrations no greater than 1 ppbV, formation of peroxides within the chamber becomes efficient as soon as the photochemistry is initiated and peroxy radicals are formed (see Figs. 1d and 4). Under low NO_x conditions Eq. 2 predicts that partitioning of RO_2 to peroxides is as efficient as ~5% after only the first 10 min of experiment, a result that contrasts strongly with findings from the high NO_x cases. Furthermore, Eq. 2 predicts that partitioning of RO_2 to peroxides reached roughly 15% by the time of the nucleation event of Experiment 5. These experimental findings further strengthen theories proposing the crucial role played by organic peroxides during the SOA formation process.

3.5 Effect of inorganic seed

A comparison of the two low NO_x experiments (5 and 7) in Table 2 shows that particle formation occurred ~30 min earlier when SO_2 gas was included in the matrix. This result could be due to slightly higher OH levels measured during Experiment 7, but is most likely a consequence of H_2SO_4 nucleation, which subsequently supplies a condensation surface for the condensable organic oxidation products (Holmes, 2007). In addition to this, seeding the chamber generated a larger number of particles than in other experiments. The peak particle number density during Experiment 7 reached roughly 2200 cm^{-3}, compared to only 410 cm^{-3} during Experiment 5. Due to the larger number of particles produced, the mean geometric aerosol diameter of the seeded SOA was slightly smaller than that produced by homogeneous nucleation, i.e. ~400 compared to ~460 nm.

Various chamber studies have shown that SOA yields generated from a VOC precursor can become enhanced in the presence of an acidic seed (Jang and Kamens, 2001; Czoschke et al., 2003; Jang et al., 2003; Limbeck et al., 2003; Gao et al., 2004; Surratt et al., 2007; Verheggen et al., 2007). Further inspection of Table 2 shows that despite the production of a greater number of particles, the aerosol yield obtained in the presence of H_2SO_4 was no greater than the yield obtained during the companion low NO_x homogeneous nucleation experiment. However, the SO_2 concentration employed during Experiment 7 was somewhat low (0.4 ppbV compared to >100 ppbV used by other workers, e.g. Edney et al., 2005; Kleindienst et al., 2006; Metzger et al., 2008b[3]); hence it is possible that the resultant [H_2SO_4] was too low to facilitate the acid seed effect. Therefore, with this in mind and with a lack of repeat seed experiments, the result of no yield enhancement for TMB-SOA in the presence of H_2SO_4 is not conclusive, but is in line with findings presented by Ng et al. for two other aromatic systems: toluene and *m*-xylene (Ng et al., 2007). A more exhaustive study investigating the effect of acid seeding on TMB-SOA has been produced recently by Metzger et al. (Metzger et al., 2008b[3]).

3.6 Time-dependent SOA growth curves

In order to help elucidate the mechanisms underlying SOA formation in the TMB system, a series of time-dependent SOA growth curves have been generated, following methods employed by Song, Ng and co-workers (Song et al., 2005; Ng et al., 2007). The time-dependent growth curves essentially comprise a plot of SOA mass formed versus the amount of VOC reacted. Figure 5a presents the growth curve for Experiment 6, a typical example of the high NO_x system (VOC/NO_x~2:1). Initial inspection reveals the significant incubation period noted previously as the chamber concentration of NO→0. The incubation period is followed by a linear increase in SOA mass with expenditure of the TMB. The growth curve eventually reaches a plateau followed by decay due to particle deposition. Growth curves for all high NO_x experiments with VOC/NO_x~2:1 (not shown) exhibit similar behaviour, with all profiles displaying similar slopes and with all nucleation events occurring within a narrow band of reacted TMB. The time-dependent growth curves for the low NO_x experiments are also linear following nucleation, but (as noted earlier) are preceded by a much shorter incubation period than those of the high NO_x systems. As an example, Fig. 5b displays the growth curve for Experiment 7.

As noted in Sects. 3.3 and 3.4 a time delay was observed between [NO]→0 and the nucleation event in high NO_x Experiments 3, 4 and 6, which was comparable in duration to the incubation period clearly evident in the growth curves of the low NO_x experiments (e.g. Fig. 5b). As shown above, the formation of peroxides in the low NO_x system is likely to be extremely efficient even very early into the experiment. Consequently, if organic peroxides are pivotal in TMB-SOA formation, the time delay observed after [NO] has reached minimal levels corresponds to the time required for the nucleating species to reach a critical gas phase concentration. It is also possible that the presence of a time delay in certain high NO_x experiments and the incubation zone in the absence of NO_x, are a consequence of the SOA forming species consisting of later stage oxidation products which form further down the oxidation chain, i.e. from further reaction of primary products (including certain peroxides, see discussion in Sect. 3.9). Growth curves displaying similar behaviour to those derived from the current study were presented by Song et al. for the *m*-xylene system (Song et al., 2005).

3.7 The gas phase organic compounds

3.7.1 The 1,3,5-trimethylbenzne atmospheric oxidation mechanism

Before reporting the observations derived from the CIR-TOF-MS measurements, we first outline the likely atmospheric oxidation processes of TMB that might lead to SOA

[3]Metzger, A., Verheggen, B., Duplissy, J., Gaeggeler, K., Dommen, J., Prevot, A. S. H., and Baltensperger, U.: Influence of sulfur dioxide on nucleation, growth rates and yield of secondary organic aerosol, in preparation, 2008b.

formation. Atmospheric oxidation of TMB may essentially be separated into two distinct pathways. One pathway is reaction via OH addition to the aromatic ring (pathway *(Pi)*) while the other involves hydrogen abstraction from a methyl group (pathway *(Pii)*). In general, the more substituted the aromatic ring, the more important the ring fragmentation route (Johnson et al., 2005; Bloss et al., 2005b). A simplified mechanism for the photochemical degradation of TMB, highlighting the most important atmospheric oxidation routes, is displayed in Fig. 6. This scheme has been constructed through an amalgamation of previous descriptions of the benzene and toluene oxidation systems (Yu et al., 1997; Atkinson, 2000; Bohn, 2001; Calvert et al., 2002; Johnson et al., 2004; Johnson et al., 2005), the MCMv3.1 TMB subset (extracted from the MCM website (http://mcm.leeds.ac.uk/MCM), Bloss et al., 2005a; Bloss et al., 2005b) and measurements made by CIR-TOF-MS during this study:

(Pi) OH Addition to the aromatic ring

The principal atmospheric oxidation route for TMB involves the addition of OH to the aromatic ring (branching ratio of 0.97 in the MCMv3.1), initially forming an OH-aromatic adduct (a trimethyl hydroxycyclohexadienyl radical; compound B in Fig. 6). In the presence of atmospheric levels of O_2 this radical is in equilibrium with its equivalent OH-aromatic-O_2 adduct (a trimethyl hydroxycyclohexadienyl peroxy radical) (C). The OH-aromatic-O_2 adduct (C) can either subsequently decompose to yield HO_2 and the ring retaining product 2,4,6-trimethylphenol (D), or most likely will undergo internal rearrangement to generate an O_2-bridged trimethyl peroxide bicyclic radical (E) (branching ratio of 0.96 in MCMv3.1). The O_2-bridged trimethyl peroxide bicyclic radical (E) can subsequently degrade through various stages of isomerisation, decomposition and scission to form the epoxy-oxy species (H) (branching ratio of 0.15 in MCMv3.1). The epoxy-oxy compound can decompose to give a variety of lower molar mass oxygenates (e.g. compounds I and J). In the atmosphere the bicyclic peroxide radical (E) will most likely undergo reaction with O_2 to form the peroxy radical equivalent (K) (branching ratio of 0.85 in MCMv3.1). The yields of initial products formed after addition of OH to

the aromatic ring of TMB in MCMv3.1 are 0.79, 0.14, and 0.04 for the trimethyl peroxide bicyclic peroxy radical (K), the epoxy-oxy species (H) and 2,4,6-trimethylphenol (D), respectively. Depending on the amount of NO_x present, the peroxide bicyclic peroxy radical (K) will degrade via a number of intermediary steps to produce a range of O_2-bridged oxygenated and nitrated compounds (compounds L–P). Some of the larger oxygenated and nitrated ring retaining products, including the multi-functional O_2-bridged species shown in Fig. 6, are likely to be sufficiently non-volatile to partition into the organic aerosol phase (Johnson et al., 2004; Johnson et al., 2005). Once inside the particle phase, these types of multi-functional compounds can take part in certain association reactions (Johnson et al., 2005). Further oxidation and ring opening processes (mainly through the oxy radical (N)) will yield an array of lower molecular mass carbonyl (including methyl glyoxal), unsaturated γ-dicarbonyl, acid and furanone species, some of which are shown in Fig. 6 (e.g. compounds Q–S). These low molecular mass ring fragmentation products have a tendency to be multi-functional and can be unsaturated, and therefore are generally more reactive than the parent TMB and can be oxidised further through reactions with OH and O_3 and NO_3. A selection of likely, further reaction products are shown in Fig. 6. Some of these products, e.g. 3-methyl maleic anhydride (citraconic anhydride) (AC) and 3,5-dimethyl-5(2H)-2-furanone (S), can be highly polar and less volatile, and hence may be able to transfer into the organic aerosol phase (Kleindienst et al., 1999; Johnson et al., 2005).

(Pii) Hydrogen abstraction from a pendant methyl group

OH initiated hydrogen abstraction from a pendant methyl group constitutes the alternative oxidation route for TMB in the atmosphere, and represents the major ring retaining pathway (other than the formation of 2,4,6-trimethyl phenol as described above). Eventually, following hydrogen abstraction, reaction with O_2, and subsequent radical reactions (e.g. with NO, RO_2, HO_2 and OH), 3,5 dimethyl benzaldehyde (W) is formed with a yield of ~0.03 according to MCMv3.1 (Bloss et al., 2005b).

3.8 Measurement of the gas phase organic compounds

Figure 7a–d displays the CIR-TOF-MS mass spectra recorded after 400 min of irradiation during Experiments 6, 3, 2 and 7, with VOC/NO_x ratios of around 2:1, 1:2, 2:1 (NO only) and 17:1, respectively. All of the mass spectra have been normalised to 10^6 primary reagent ion counts (i.e. the sum of the H_3O^+ and $H_3O^+.H_2O$ signals) and have been background subtracted. Consequently, all signals stated here are quoted in units of normalised counts per second i.e. ncps (de Gouw et al., 2003).

During a typical high NO_x chamber experiment (and depending on the drift cell conditions employed) around 60 peaks were recorded in the mass spectra between m/z 0 and 300, with around 30 peaks possessing a mass greater than that of the precursor VOC (m/z 121). In contrast, roughly 50 significant features were recorded during the low NO_x experiments, with around 20 of those possessing a mass greater than that of the precursor. It should be noted, however, that this difference could be attributed to the use of a lower precursor concentration during the low NO_x studies where detection limits of the instrument become an issue (see Wyche et al., 2007 for further information regarding detection limits). The number of spectral features quoted here includes features present due to fragment ions as well as parent ions, and hence does not necessarily represent the total diversity of organic species in the chamber. For brief periods during certain experiments, the electric field applied across the collision cell in the CIR-TOF-MS drift tube was increased to produce more energetic collisions, and thus to identify and help exclude any possible molecular ion water cluster products (i.e. $MH^+.(H_2O)_n$).

The major spectral features common to all experiments are listed in Table 4 along with, where possible, a tentative compound assignment. Table 4 also gives a chamber "appearance time" for each compound, defined as the time at which the signal for a given spectral feature exceeds the mean background signal plus three times its standard deviation. All compound assignments have been made using a combination of information, namely accurate mass measurements, appearance time, subsequent

temporal profile, and data available from the MCMv3.1 box model simulations (see Rickard et al., 2008).

3.8.1 Behaviour of the gas phase organics under high NO_x conditions

As a focus for discussion, the evolution of the entire measured VOC system of Experiment 6 is presented in Fig. 8. General features of note include the appearance of most species within the first 50–100 min of the experiment, including many high mass oxidation products. The high NO_x photooxidation system of TMB is also characterised by a peak in concentration of the heavier species around the mid-point of the experiment (~200–300 min). The lower molecular mass features demonstrate a continual rise in intensity up to the end of the experiment.

Looking more closely at the features recorded by CIR-TOF-MS (Table 4), it is possible to follow the system evolution as outlined in Fig. 6. Two of the earliest compounds to appear in the oxidation chain are the ring retaining compounds, 2,4,6-trimethylphenol (D) and 3,5-dimethylbenzaldehyde (W). Both of which were measured in the chamber as protonated parent ions, i.e. m/z 137 and 135, respectively. 2,4,6-trimethylphenol and 3,5-dimethylbenzaldehyde were measured with peak concentrations of 0.6 and 7 ppbV, respectively.

As noted in Sect. 3.7.1, the majority of mass transit in the TMB oxidation system occurs via addition of OH to the aromatic ring followed by production of the trimethyl peroxide bicyclic radical (E) and its peroxy radical counterpart (K). Various subsequent pathways shown in Fig. 6 can lead to an array of O_2-bridged aromatic compounds (L–P). We report here the first firm evidence for the existence of these O_2-bridged species along with documentation of their real-time evolution, as measured by CIR-TOF-MS. As summarised in Table 4, peaks consistent with the O_2-bridged nitrate (L), diol (O) and ketone (P) were recorded at m/z 232, 169 and 185, respectively. Two fragment ions of the nitrate were also measured (at m/z 214 and 109), as was a signal tentatively assigned to be the aromatic ring fragment of the O_2-bridged species (m/z 125). No ion corresponding to the protonated O_2-bridged peroxide (M) was measured. Comparison

of the measured temporal profiles of the O_2-bridged species with simulations using a chamber box model incorporating detailed TMB degradation chemistry taken from the MCMv3.1 is discussed in the companion modelling paper (Rickard et al., 2008).

Due to relatively high levels of NO early in the experiment, the O_2-bridged nitrate (L) is the first of the triumvirate to appear in the chamber, at ∼10–50 min. The O_2-bridged nitrate is formed in relatively high yield when compared to the other aromatic systems (Bloss et al., 2005b). As the chamber matrix evolves and levels of HO_2 and RO_2 increase, the O_2-bridged diol and ketone (and presumably the peroxide (M): see Rickard et al., 2008) are produced, appearing roughly together at ∼40–60 min.

The concentration-time profiles of the measured O_2-bridged bicyclic species are shown in Fig. 9a. The primary bicyclic nitrate exists in a state of production whilst NO is present in the chamber, up to a peak near 250 min, followed by decay as the precursor TMB is consumed and as chamber NO_x falls towards zero. The O_2-bridged diol and ketone follow a similar profile to the nitrate early in the experiment but continue on a steady rise as HO_2 and RO_2 become more prevalent within the chamber.

According to the mechanism outlined in Fig. 6, the O_2-bridged ketone (P) and alkoxy radical (N) act as conduits for further mass transit through the oxidation system. Both compounds are liable to undergo ring cleavage to yield an array of lower molecular mass oxygenated and nitrated compounds, the first and most abundant of which are methyl glyoxal (Q) and 3,5-dimethyl-5(2H)-2-furanone (S), measured as protonated parent ions at m/z 73 and 113, respectively. A variety of oxygenated species, all of nominal mass 112, appear in the TMB oxidation chain and were measured collectively at m/z 113 (i.e. protonated) by CIR-TOF-MS. Along with 3,5-dimethyl-5(2H)-2-furanone, laboratory studies have identified these to be the furanones, 3,5-dimethyl-3(2H)-2-furanone (AF) and 3-methyl-furan-2,5-dione (methyl maleic anhydride) (AC), and the -dicarbonyl 2-methyl-4-oxo-2-pentenal (R) (Smith et al., 1999). Also observed here in the chamber matrix was a fourth furanone, 3-methy-5-methylidene-5(2H)-2-furanone, measured at m/z 111 (AE) (Smith et al., 1999).

Both methyl glyoxal and the m/z 113 compounds are amongst the first oxidation

products to appear in the chamber (after ∼3–30 min), being formed via a series of highly reactive radical intermediates during the early, NOx dominated stages of the high NO_x experiment. As shown in Fig. 9b, the concentrations of methyl glyoxal, 3-methy-5-methylidene-5(2H)-2-furanone and the m/z 113 species rise rapidly to peaks of ∼110, 30 and 65 ppbV, at roughly 320, 450 and 170 min, respectively. Eventually the chemistry generating these oxidation products reaches steady state, as indicted by the observed concentration plateaus.

Throughout the experiment methyl glyoxal, methyl-5-methylidiene-5(2H)-2- furanone and the m/z 113 species were amongst the most dominant features of the mass spectrum, being produced first via the alkoxy radical and the bicyclic nitrate, and subsequently through the HO_2 and RO_2 controlled pathways. At peak concentrations the (mass percent) VOC yields (Y_{VOC}) for these compounds were estimated to be ∼20, 8 and 40%, respectively, accounting for a significant fraction of mass within the system.

As the oxidation process progressed a multitude of organic species with a variety of functional groups were formed within the chamber, many of which were detected by CIR-TOF-MS (see Table 4). Figure 9c gives the concentration-time profiles for three such compounds formed following ring cleavage, the multifunctional tertiary products 2-methyl-4-oxo-pent-2-enoic acid and 3-acetyl-2-methyl-oxirane-2-carbaldehyde (measured together at m/z 129) and hydroxy acetone (m/z 75). Collision energy studies have shown that 2-methyl-4-oxo-pent-2-enoic acid also undergoes a small amount of dehydration following PTR to yield a fragment of m/z 111. Also given in Fig. 9c is the signal measured at m/z 43, a generic marker for carbonyls using the PTR-MS technique (Blake et al., 2006). All such later stage oxidation products displayed similar behaviour, a steady rise to plateau roughly coinciding with peak aerosol mass. Strong signals corresponding to nitrated VOCs (even m/z number and low mass excess) were also measured further down the oxidation chain. These included peroxy acetyl nitrate (PAN) (m/z 46, Hansel and Wisthaler, 2000) and two unidentified compounds of m/z 96 and 136. Signals corresponding to pyruvic acid (m/z 89) and formaldehyde (m/z 31), two potential monomer units for the TMB oligomer (Kalberer et al., 2004),

were also measured in all experiments.

Further inspection of Table 4 shows that a number of other simple organic acids were observed in the gas phase, including hydroxy acetic acid (m/z 77), acetic acid (m/z 61) and formic acid (m/z 47). As shown in Fig. 9d and Table 4, the various late stage acids appeared in the chamber ~20–200 min after lights on. Concentrations of hydroxy acetic acid rose steadily to a peak of around 30 ppbV at 400 min (Y_{VOC}=6%) followed by a steady decline. Both formic and acetic acid levels continued to rise throughout Experiment 6 as the system became more oxidised, with concentrations eventually reaching 100–120 ppbV (Y_{VOC}~11 and 16%, respectively). It should be noted that during "blank" experiments (no precursor VOC), both formic and acetic acid were observed in the gas phase following liberation from the illuminated chamber walls. After ~7 h of blank experiment ~10 ppbV of both formic and acetic acid was measured; hence concentrations quoted here constitute an upper limit and should be considered with care. However, Fisseha and colleagues (Fisseha et al., 2004) recently recorded similar gas phase concentrations of formic acid during TMB photooxidation (~80 ppbV after 9 h), along with significant levels within the aerosol (~15 μg m^{-3} at peak aerosol concentration). They presented lower acetic acid concentrations than were measured here (~30 ppbV), with differences most likely explained by potential contribution to mass channel 61 from other species in the CIR-TOF-MS measurements (primarily fragment ions derived from other organic acids).

3.8.2 Variation of the VOC/NO_x ratio under high NO_x conditions

When NO_x was initially introduced only in the form of NO (Experiment 2), the distribution and variety of ions within the mass spectrum and their concentration-time profiles were generally very similar to those of other experiments with initial VOC/NO_x~2:1. The main exception to this was a delay in the appearance times of most compounds, corresponding to the time required to liberate HONO from reactions on the chamber walls and hence for the radical chemistry to initiate. Also, the oxidation products reached higher peak concentrations due to the enhanced level of starting material, but ultimately

achieved similar yields to the other experiments of VOC/NO_x~2:1 (see Table A2).

The behaviour of the VOC component of the chamber differed more significantly when the VOC/NO_x ratio was reversed to a value of ~1:2. The most obvious point of note was that despite generally exhibiting similar temporal behaviour to other high NO_x experiments, the oxidation products of the reverse system took significantly longer to appear and achieve peak concentrations.

3.8.3 Variation of the VOC/NO_x ratio, low NO_x conditions

Following observations of the aerosol phase, the composition and behaviour of the gas phase organics of the low NO_x systems (Experiments 5 and 7, VOC/NO_x~16:1) show significant differences to those of the high NO_x experiments. Along with exhibiting significantly earlier nucleation events, due to the presence of the HONO radical source Experiments 5 and 7 were also characterised by the appearance of most oxidation products much sooner than in all other experiments (see Table 4). Figure 10 shows that, once present in the chamber, the TMB oxidation products exhibited significantly different temporal behaviour under low NO_x conditions when compared to other experiments. The majority of primary oxidation products were observed to rise more gradually from "lights on" to a concentration plateau, rather than a distinct peak. Consequently, the point of maximum concentration often occurred later than in other experiments, e.g. methyl glyoxal (m/z 73) and the m/z 113 compounds reached maxima around 70–80 min later than in Experiment 6, achieving ~50 and 20 ppbV, respectively. Correspondingly the later stage oxidation products also presented different temporal profiles. As seen in Fig. 10c and d, the tertiary products presented more linear growth profiles early in the experiment, being produced more rapidly due to the presence of an OH source. The "start-up" lag seen in other experiments, corresponding to the time required to establish the OH cycle, is absent. During low NO_x experiments, the tertiary products were often characterised by linear profiles due to a roughly constant level of oxidant.

Most VOC yields (determined for the calibrated compounds) during the low NOx

experiments were similar in magnitude to those of the high NOx experiments of VOC/NO_x~2:1, with some significant exceptions. Hydroxy acetic acid, acetic acid and formic acid yields obtained during low NOx experiments were on average significantly larger than those of high NOx experiments, i.e. 14, 33 and 49% compared to 4, 15 and 13%, respectively. Yields for methyl glyoxal and the m/z 113 compounds were slightly lower under low NOx conditions, namely ~20 and 30%, respectively.

3.8.4 Elucidating the gas phase oxidation mechanisms

In order to evaluate the chemical mechanism underlying the TMB photooxidation system, at the conclusion of certain experiments chamber lights were switched off and the total chamber ozone was titrated from the system with the addition of excess NO to the matrix. During Experiments 6 and 7 the chamber lights were switched off at 460 and 550 min, respectively, with the addition of NO some 60 and 30 min later. The effect of this "dark phase" on the inorganic components of the matrix and the VOCs for Experiments 6 and 7 can be seen in Figs. 1a and d, 9 and 10.

During the dark phase the photochemically driven pathways become 'switched off' as photolysis and OH production from both ozone and HONO cease. Also, as the chamber ozone is titrated away, chemistry occurring via ozonolysis reactions becomes negligible. Consequently, the system chemistry is switched from a regime where reactions of RO_2 are controlled by OH and HO_2 to one in which the majority of RO_2 species are removed from the system following reaction with the injected NO. This results in a "burst" in production of NO_2 and to a minor extent nitrogenated and carbonyl compounds. Manipulating the chemistry in this manner and observing the resultant effect on the VOC evolution provides key insight into the chemistry involved.

The concentration-time profile of the peroxide bicyclic ketone, seen in Fig. 9a, began to fall significantly when chamber lights were switched off, suggesting that its production must result from reactions involving RO_2, HO_2 and OH as detailed in Fig. 6. As the photolytic formation of radicals was "switched off" under dark phase conditions, production of the bicyclic ketone was no longer possible and the chamber concentration

began to decay due to the instability of this species. Conversely during the dark phase, the fall in concentration of the bicyclic nitrate was arrested before levelling off to plateau as its major loss process (i.e. photolysis) was switched off.

Following the addition of NO to the chamber a significant increase in the signal measured at m/z 113 was observed. This response is essentially a consequence of the parent O_2-bridged species decomposing through ring opening pathways to yield various (isobaric) oxygenated products. For example following the photooxidation mechanism outlined in Fig. 6, it is likely that the peroxide bicyclic ketone decays via several intermediate steps to 3,5-dimethyl-5(2H)-2-furanone, verifying this compound's significant contribution to the signal measured at m/z 113. Such findings highlight the importance of reaction routes involving the bicyclic ketone and nitrate species during the early stages of the experiment in the production of other potentially crucial SOA forming oxidation products (see Sect. 3.9).

3.9 Principal component analysis

As noted by Baltensperger et al. (Baltensperger et al., 2005) the VOCs observed in the oxidation of TMB can be separated into several distinct categories according to their temporal profiles. In order to better identify trends within the time series data, a Principal Component Analysis (PCA, Martens and Næs) was carried out for each experiment. PCA is an exploratory data analysis technique that will summarise correlated time behaviour of certain masses into a set of principal components. Each principal component consists of a pair of vectors: the scores vector (depicting time related behaviour) and the loadings vector (representing how strongly this behaviour is represented on each of the masses). The PCA algorithm will first find the strongest collective time trend in the data and its associated mass spectrum, followed by the second strongest and so on. Consequently, it may therefore be possible to represent the whole experiment with only a few principal components. Ultimately the PCA can be used to identify which compounds are related in the oxidation system.

Generally, during each of the PC analyses the vast majority of the temporal variability

was captured by the first three principal components (PC1 accounted for ∼75–95% of the variance, PC2 ∼4–22% and PC3 only ∼0.6–1.5%). As an example of the high NO_x data, the scores and loading plots obtained from a PCA conducted for Experiment 6 are given in Fig. 11a. The scores plots generated for PC1 for each high NO_x experiment exhibited roughly the same pattern, i.e. a sigmoidal rise to peak and plateau. The most significant masses comprising the corresponding loadings vector were m/z 43 (carbonyl marker), 46 (PAN marker), 61 (acetic acid), 73 (methyl glyoxal), 77 (hydroxyl acetic acid), 87 (unidentified), 111 (3-methyl-5-methylidiene-5(2H)-2-furanone) and 185 (the O_2-bridged ketone). All of these masses (except m/z 185) constitute secondary or tertiary oxidation products of the TMB system (although methyl glyoxal also constitutes a primary product). The PAN and acetic acid signals were the greatest contributors towards the first principal component in all high NO_x experiments.

The scores generated for PC2 were characterised by a rapid rise to peak followed by a similarly steep decay to steady state. The most significant corresponding loadings were m/z 45 (methyl glyoxal fragment), 73 (methyl glyoxal), 85 (m/z 113 fragment), 113 (isobaric furanone and δ–dicarbonyl ring opening products), 125 (bicyclic fragment), 135 (3,5-dimethyl benzaldehyde), 214 and 232 (bicyclic nitrate). These compounds constitute the primary oxidation products of the TMB oxidation system. The m/z 73 and 113 signals were the greatest contributors towards the second principal component in all high NO_x experiments. PC3 accounts for very little of the variance within all experiments, only ∼1% and is composed mainly of three significant loadings corresponding to masses 47, 61 and 113.

The PCA for low NO_x Experiment 7 is shown in Fig. 11b. Comparison of the scores plots with those of Experiment 6 (Fig. 11a) demonstrates the dramatic differences in the temporal behavior of the oxidation products, with no evidence of an incubation period in the VOC chemistry, i.e. the primary, secondary and tertiary products of oxidation appear in the system early on in experiment. PC1 for the low NO_x system is primarily composed of the same compounds as in the high NO_x system with, however, a different distribution of abundances. Under low NO_x conditions m/z 45, 46, 73, and 111 all show

significantly lower contributions to the secondary products, although m/z 61 remains the greatest contributor, suggesting a more dominant role for acetic acid in the absence of NO_x. In contrast to this, PC2 is composed of a slightly different set of masses with distinctly different abundances. Masses 45, 73, 97 (unidentified), 125, 135 and particularly 111 all give stronger contributions than in the high NO_x experiments. Contrary to the high NO_x system, the second principal component also contains contributions from masses 101 (unidentified), 129 (organic acid), 139 (organic peroxide), 169 (O_2-bridged diol) and 185. These findings suggest that although ultimately the same end stage oxidation products are reached, during the early stages of the low NO_x experiments (i.e. approximately around the time of nucleation) the system chemistry is somewhat different, generating an organic gas phase matrix that is more strongly dominated by the primary O_2-bridged bicyclics, methyl glyoxal and the m/z 113 compounds. This finding implies therefore that such species may play some role in the formation of aromatic SOA.

3.10 Identification of compounds contributing to SOA formation and growth

Although a large fraction of SOA mass remains to be identified, recent studies into the composition of aerosol formed from aromatic compounds has highlighted the presence of a discrete set of organic species originating directly from gas phase oxidation of the precursor. Of these compounds previously identified within the aerosol, several were measured (or their analogous counterparts were measured) in the gas phase during the present study, including 3,5-dimethylbenzaldehyde (Hamilton et al., 2003) from the ring retaining route, certain of the isobaric m/z 113 furanones (Forstner et al., 1997; Hamilton et al., 2003) and methyl glyoxal (Kalberer et al., 2004) from the ring opening route, along with the later stage decay products hydroxy acetone, glycoaldehyde (Cocker III et al., 2001), formic acid and acetic acid (Fisseha et al., 2004).

For the gas phase species to take part in the SOA formation process, first of all their presence in the chamber must coincide with or precede the onset of nucleation. By the time of nucleation in each high NO_x experiment, virtually all of the measured

organic species had appeared within the chamber and hence (where possible) were available for partitioning. In contrast, a more select group of only 13 spectral features were present in the mass spectra of both low NO_x experiments prior to nucleation, and hence available to the aerosol. This result implies that the early stage aerosol in the low NO_x systems may be less compositionally diverse.

Several of the "early" features of the low NO_x system were observed within the first few minutes of experiment: these include, the O_2-bridged nitrate (at m/z 232, 214 and 109), diol (m/z 169), and fragment (m/z 125), methyl glyoxal (m/z 73) and the m/z 113 ring opening compounds. Other notable cases of early appearance include, the O_2-bridged ketone, 3,5-dimethyl benzaldehyde, hydroxy acetic acid, acetic acid and the carbonyl marker (m/z 185, 137, 77, 61 and 43, respectively). As some organic compounds are not easily ionised using the proton transfer reaction technique (e.g. peroxides) and as detection limits may have excluded some compounds, it is not possible at present to conclusively assign the nucleating species. However, with only the above listed compounds measured before nucleation in every experiment, it is possible that at least some of these species will be of some importance in the SOA formation process.

The appearance times of the majority of the oxidation products during low NO_x Experiment 5 were slightly later than in the corresponding low NO_x Experiment 7, as was the time of the nucleation event. Although nucleation during Experiment 7 was influenced by the presence of the inorganic seed particles, the slightly higher [OH] would have facilitated faster oxidation and therefore earlier SOA formation. A similar trend was also noted when the VOC/NO_x ratio was set to ~1:2. Here the appearance times of most of the TMB oxidation products were significantly delayed with respect to all other experiments. For example, methyl glyoxal (m/z 73) and the m/z 113 compounds appeared ~ 30 minutes later and the signals observed in mass channels representative of the primary bicyclic compounds (e.g. m/z 214, 109 and 125) a full hour later than in Experiment 6 (see Table 4 for further comparison). Subsequently methyl glyoxal, the m/z 113 species.

As noted above, the low NO_x system was characterised by an enhancement in the yields for certain gas phase species, including several organic acids. Hydroxy acetic acid, acetic acid and formic acid yields during the low NO_x experiments were on average ~3.5, 2.2 and 3.7 times larger than during the high NO_x experiments of VOC/NO_x~2:1 and 1.5, 2.8 and 6.8 times larger than during the high NO_x Experiment 3 of VOC/NO_x~1:2. As Experiment 3 was conducted with the same initial TMB concentration as the two low NO_x experiments, yield concentration artefacts suggested by some authors can be ruled out (Ng et al., 2007).

Considering that these organic acids were available in the gas phase from early on in all experiments it is possible that their enhanced gas phase yields were at least in some part responsible for the observed increase in aerosol yields obtained under low NO_x conditions, thus supplying confirmation to recent reports concerning the importance of organic acids in the composition of SOA. For example, Fisseha et al. (2004) have shown that around the point of maximum aerosol number density, organic acids comprised as much as 43% of aerosol mass. As well as simply being detected in the aerosol phase, evidence has come to light implicating that such organic acids may become incorporated into polymer-like structures found within SOA (Gross et al., 2006; Kalberer et al., 2006). Other findings published recently by various authors indicate that an acidic environment is crucial for the formation of such polymer species via various mechanistic pathways (Jang and Kamens, 2001; Czoschke et al., 2003; Limbeck et al., 2003; Gao et al., 2004; Tolocka et al., 2004; Northcross and Jang, 2007; Surratt et al., 2007; Verheggen et al., 2007). However as noted above, no distinct difference in aerosol yield was obtained between the homogeneous nucleation Experiment 5 and the acid-seeded Experiment 7. It would seem reasonable to assume therefore that if enough SO_2 was present to cause an acid seed effect and that the observed enhancement in aerosol yield is related to the enhancement in yields of the gaseous organic acid, then the levels of acids produced under low NO_x conditions were large enough to facilitate any acid-catalysed polymerisation without the need for the inorganic acid surface. Alternatively, the organic acids may contribute to SOA mass without involvement

in additional acid-catalysed polymerisation.

With no calibration method or reliable kinetic information available for the primary bicyclic compounds, it is not possible at present to derive their absolute concentrations or yields. However, pseudo yields may be derived by applying the CIR-TOF-MS sensitivity for a structurally similar compound, and in this instance *m*-tolualdehyde was employed. Regardless of the absolute values obtained, a ratio of the yields for the low versus high NO_x experiments can be used to infer the importance of the primary bicyclic species in the SOA formation process. Using data from experiments 6 and 7, the ratio of pseudo yields obtained for $\sum(m/z$ 109+214+232) was 1.36, suggesting a slight enhancement in the bicyclic nitrate under low NO_x conditions. The corresponding ratios for m/z 169 and 185 were 5.97 and 2.89, respectively, indicating much stronger production of the O_2-bridged diol and ketone in the absence of NO_x. Similar yield ratios were obtained for the measured O_2-bridged compounds when comparing high and low NO_x experiments with the same starting concentration of TMB (i.e. Experiments 3 and 7, respectively).

As with the organic acids, the increased yield of the O_2-bridged compounds could explain the enhanced SOA yield observed under low NO_x conditions, particularly when supported with evidence of their appearance in the chamber prior to nucleation in each experiment. Furthermore, modelling studies by Stroud et al. (Stroud et al., 2004) and Johnson et al. (Johnson et al., 2005) have shown that the analogous O_2-bridged nitrate (as well as some of the other multi-functional O_2-bridged products) in the toluene system and the O_2-bridged ketone in the TMB system are liable to undergo partitioning to the aerosol phase and make a significant contribution to the simulated SOA mass.

Using the methodology applied by Ng et al. (Ng et al., 2006) it is possible to glean further information regarding which species contribute to SOA growth via close inspection of their time series profiles. The concentration peaks of the O_2-bridged nitrate, the unidentified nitrate at m/z 136 and the isobaric m/z 113 oxygenates roughly coincide with the nucleation event: indeed it was observed that a shift in the time of peak was matched by a corresponding shift in the time of nucleation. Plotting the mass of these

compounds consumed (or lost) after their concentration peak versus SOA mass produced (up to the point of maximum mass) gives a strong correlation. An example of this is given in Fig. 12a and b for the nitrate of m/z 136.

The correlation plots of O_2-bridged nitrate for experiments conducted under high NO_x conditions are similar to those conducted under low NO_x (plots for Experiments 6 and 7, given in Fig. 13a and b). The correlation between mass lost and SOA mass produced indicates that the O_2-bridged nitrate contributes to SOA growth, either by direct partitioning or via further reaction generating condensable products. A steeper line fit during the low NO_x experiment suggests more rapid contribution in the absence of NO_x (see Fig. 13 for line fit coefficients). The presence of a non-zero intercept on the ordinate axis ($\sim$14–24 $\mu g\,m^{-3}$) implies that a given amount of SOA mass was formed before any contribution to SOA growth from the O_2-bridged nitrate.

Correlation plots for loss of the nitrate at m/z 136 (not shown) and the m/z 113 compounds under low NO_x conditions (Fig. 13d) are very similar to those of the bicyclic nitrate. Hence, similarly under low NO_x conditions it appears that the nitrate of m/z 136 and one or more of the compounds measured at m/z113 contribute to SOA growth once SOA has formed. Under high NO_x the corresponding correlations are very strong (Figs. 12b and 13c), but as with the bicyclic nitrate the gradient of the line fit remains steepest under low NO_x conditions. For both m/z 136 and 113 under high NO_x conditions, there exists a small non-zero intercept on the abscissa, suggesting that either no or very little SOA mass was formed prior to loss of these compounds from the gas phase. This result suggests that as well as contributing to SOA growth, the nitrate of m/z 136 and the compounds of m/z 113 may play some role in particle formation under high NO_x conditions.

It would seem from the evidence presented here that the O_2-bridged nitrate and m/z 113 compounds contribute towards SOA growth, along with compounds such as the unidentified nitrate (m/z 136), the O_2-bridged diol and the lower molecular mass organic acids. However, evidence obtained from the low NO_x experiments suggests that the presence of other species is required to initiate nucleation. From the discussion

presented here two likely candidates for the role of "nucleating species" are:

1. O_2-brigded ketone. The bicyclic ketone is present in the gas phase before nucleation in all experiments and has a temporal profile that grows in line with SOA mass. Furthermore, the higher gas phase yield for the bicyclic ketone under low NO_x conditions is matched by an ultimately higher aerosol yield. This suggestion also supports modelling studies of Johnson et al., who propose significant partitioning of the O_2-bridged ketone to the aerosol phase in their gas-aerosol coupled box model (Johnson et al., 2005).

2. O_2-bridged peroxide. As discussed in Sects. 3.3–3.5 there exists evidence from this work and from that of previous studies, that organic peroxides may play a significant role in SOA formation and growth. Considering the mechanism outlined in Fig. 6, the most dominant organic peroxide available in the early chamber matrix is the O_2-bridged peroxide (compound M), formed from the parent O_2-bridged peroxy radical (K) reacting with HO_2. No direct measurements of the bicyclic peroxide were made within this study; however from observations of the peroxy radical behaviour and from the partitioning theory of equation E2 (see Fig. 3), it is highly likely that the O_2-bridged peroxide would have been present in the chamber prior to nucleation in each experiment. We discuss the potential role of the O_2-bridged peroxide in SOA formation and growth in more detail in a companion modelling paper, utilising comparison between the measurements described here and modelling results obtained from a chamber box model (Rickard et al., 2008).

4 Conclusions

The work presented here constitutes the most comprehensive set of gas phase measurements made to date describing the unexplored composition and evolution of the organic oxidation products of an anthropogenic SOA precursor. VOC measurements

made by CIR-TOF-MS include gas phase oxidation products with the highest mass observed in aerosol simulation experiments so far. Furthermore, the high mass resolution available in TOF-MS has helped us to identify certain primary bicyclic oxidation products, measurements of which have not previously been reported in the literature, which crucially give support to our current understanding of aromatic hydrocarbon oxidation. Moreover, compound appearance times, temporal behaviour and enhanced yields under low NO_x conditions (that correlate with enhanced SOA yields), imply a role for the oxygen-bridged species and certain organic acids in the growth of TMB-SOA.

Variation of the initial chamber NO_x conditions and time-dependent SOA growth curves indicate a potential role for various other (multi-functional) gas phase organics in SOA growth, which appear at various stages in the oxidation chain. These include, 3,5-dimethylbenzaldehyde, nitrogenated compounds, furanone and dicarbonyl type species as well as simple low molecular weight organic acids. Along with methyl glyoxal, the O_2-bridged ketone and the m/z 113 isobaric furanone and δ-dicarbonyl ring opening products act as "mass conduits" through which a significant portion of mass transit occurs. Such strong markers could be used during gas phase measurements to "fingerprint" SOA formation episodes in the real atmosphere.

References

Atkinson, R.: Atmospheric chemistry of VOCs and NO_x, Atmos. Environ., 34, 2063–2101, 2000.

Baltensperger, U., Kalberer, M., Dommen, J., Paulsen, D., Alfarra, M. R., Coe, H., Fisseha, R., Gascho, A., Gysel, M., Nyeki, S., Sax, M., Steinbacher, M., Prevot, A., Sjogren, S. H. S., and Weingartner, E.: Secondary organic aerosols from anthropogenic and biogenic precursors, Faraday Discuss., 130, 265–278, 2005.

Blake, R. S., Whyte, C., Hughes, C. O., Ellis, A. M., and Monks, P. S.: Demonstration of Proton-Transfer Reaction Time-of-Flight Mass Spectrometry form Real-Time Analysis of Trace Volatile Organic Compounds, Analytical Chemistry, 76, 3841–3845, 2003.

Blake, R. S., Wyche, K. P., Ellis, A. M., and Monks, P. S.: Chemical ionization reaction time-of-flight mass spectrometry: Multi-reagent analysis for determination of trace gas composition, I. J. Mass Spectrom., 254(1–2), 85–93, 2006.

Bloss, C., Wagner, V., Bonzanini, A., Jenkin, M. E., Wirtz, K., Martin-Reviejo, M., and Pilling, M. J.: Evaluation of detailed aromatic mechanisms (MCMv3 and MCMv3.1) against environmental chamber data, Atmos. Chem. Phys., 5, 623–639, 2005a, http://www.atmos-chem-phys.net/5/623/2005/.

Bloss, C., Wagner, V., Jenkin, M. E., Volkamer, R., Bloss, W. J., Lee, J. D., Heard, D. E., Wirtz, K., Martin-Reviejo, M., Rea, G., Wenger, J. C., and Pilling, M. J.: Developement of a detailed chemical mechanism (MCMv3.1) for the atmospheric oxidation of aromatic hydrocarbons, Atmos. Chem. Phys., 5, 641–664, 2005b, http://www.atmos-chem-phys.net/5/641/2005/.

Bohn, B.: Formation of Peroxy Radicals from OH-Toluene Adducts and O_2, J. Phys. Chem., A105, 6092–6101, 2001.

Calvert, J. G., Atkinson, R., Becker, K. H., Kamens, R. M., Seinfeld, J., Wallington, T. J., and Yarwood, G.: The Mechanisms of Atmospheric Oxidation of Aromatic Hydrocarbons, Oxford University Press, 2002

Cocker III, D. R., Mader, B. T., Kalberer, M., Flagen, R. C., and Seinfeld, J. H.: The effect of water on gas-particle partitioning of secondary organic aerosol: II. *m*-xylene and 1,3,5-trimethylbenzene photooxidation systems, Atmos. Environ., 35, 6073–6085, 2001.

Czoschke, N. M., Myoseon, J., and Kamens, R. M. : Effect of acidic seed on biogenic secondary organic aerosol growth, Atmos. Environ., 37, 4287–4299, 2003.

de Gouw, J. A., Goldan, P. D., Warneke, C., Kuster, W. C., Roberts, J. M., Marchewka, M., Bertman, S. B., Pszenny, A. A. P., and Keene, W. C.: Validation of proton transfer reaction-mass spectrometry (PTR-MS) measurements of gas-phase organic compounds in the atmosphere during the New England Air Quality Study (NEAQS) in 2002, J. Geophys. Res.-Atmos., 108(D21), 4682, doi:10.1029/2003JD003863, 2003.

Derwent, R. G., Jenkin, M. E., Passant, N. R., and Pilling, M. J.: Photochemical ozone creation potentials (POCPs) for different emission sources of organic compounds under European conditions estimated with Master Chemical Mechanism, Atmos. Environ., 41, 2570–2579, 2007a.

Derwent, R. G., Jenkin, M. E., Passant, N. R., and Pilling, M. J.: Reactivity-based strategies for photochemical ozone control in Europe, Environ. Sci. Policy, 10, 445–453, 2007b

Derwent, R. G., Jenkin, M. E., Saunders, S. M., Pilling, M. J., Simmonds, P. G., Passant, N. R., Dollard, G. J., Dumitrean, P., and Kent, A.: Photochemical ozone formation in north west Europe and its control, Atmos. Environ., 37, 1983–1991, 2003.

Dommen, J., Metzger, A., Duplissy, J., Kalberer, M., Alfarra, M. R., Gascho, A., Weingartner, E., Prevot, A. S. H., Verheggen, B., and Baltensperger, U.: Laboratory observation of oligomers in the aerosol from isoprene/NOx photooxidation, Geophys. Res. Lett., 33(13), L13805, 2006.

Edney, E. O., Kleindienst, T. E., Jaoui, M., Lewandowski, M., Offenberg, J. H., Wang, W., and Claeys, M.: Formation of 2-methyl tertrols and 2-methylglyceric acid in secondary organic aerosol from laboratory irradiated isoprene/NO_x/SO_2/air mixtures and their detection in ambient $PM_{2.5}$ samples collected in the eastern United States, Atmos. Environ., 39, 5281–5289, 2005.

Finlayson-Pitts, B. J. and Pitts Jr., J. N.: Chemistry of the Upper and Lower Atmosphere, Academic Press, 2000.

Fisseha, R., Dommen, J., Sax, M., Paulsen, D., Kalberer, M., Maurer, R., Hofler, F., Weingartner, E., and Baltensperger U.: Identification of Organic Acids in Secondary Organic Aerosol and the Corresponding Gas Phase from Chamber Experiments, Analytical Chemistry, 76(22), 6535–6540, 2004.

Fleming, Z. L., Monks, P. S., Rickard, A. R., Bandy, B. J., Brough, N., Green, T. J., Reeves, C. E., and Penkett, S. A.: Seasonal dependence of peroxy radical concentrations at a Northern hemisphere marine boundary layer site during summer and winter: evidence for radical activity in winter, Atmos. Chem. Phys., 6, 5415–5433, 2006b, http://www.atmos-chem-phys.net/6/5415/2006/.

Fleming, Z. L., Monks, P. S., Rickard, A. R., Heard, D. E., Bloss, W. J., Seakins, P. W., Still, T. J., Sommariva, R., Pilling, M. J., Morgan, R., Green, T. J., Brough, N., Mills, G. P., Penkett, S. A., Lewis, A. C., Lee, J. D., Saiz-Lopez, A., and Plane, J. M. C.: Peroxy radical chemistry and the control of ozone photochemistry at Mace Head, Ireland during the summer of 2002, Atmos. Chem. Phys., 6, 1–22, 2006a, http://www.atmos-chem-phys.net/6/1/2006/.

Forstner, H. J. L., Flagan, R. C., and Seinfeld, J. H.: Secondary Organic Aerosol from Photooxidation of Aromatic Hydrocarbons: Molecular Composition, Environ. Sci. Technol., 31, 1345–1358, 1997.

Friedrich, R., and Obermeier, A.: Anthropogenic Emissions of Volatile Organic Compounds:

Reactive Hydrocarbons in the Atmosphere. H. C. N. London, Academic Press, 2–38, 1999.
Gao, S., Ng, N. L., Keywood, M., Varutbangkul, V., Bahreini, R., Nenes, A., He, J., Yoo, K. Y., Beauchamp, J. L., Hodyss, R. P., Flagan, R. C., and Seinfeld, J. H.: Particle Phase Acidity and Oligomer Formation in Secondary Organic Aerosol, Environ. Sci. Technol., 38, 6582–6589, 2004.
Green, T. J., Reeves, C. E., Fleming, Z. L., Brough, N., Rickard, A. R., Bandy, B. J., Monks, P. S., and Penkett, S. A.: An improved dual channel PERCA instrument for atmospheric measurements of peroxy radicals, J. Environ. Monitor., 8, 530–536, 2006.
Grosjean, D.: Insitu organic aerosol formation during a smog episode- estimated production and chemical funstionality, Atmos. Environ., 26A, 953–963, 1992.
Gross, D. S., Galli, M. E., Kalberer, M., Prevot, A. S. H., Dommen, J., Alfarra, M., Duplissy, J., Gaeggeler, K., Gascho, A., Metzger, A. and Baltensperger, U.: Real-Time Measurement of Oligomeric Species in Secondary Organic Aerosol with the Aerosol Time-of-Flight Mass Spectrometer, Analytical Chemistry, 2006.
Hamilton, J. F., Lewis, A. C., Bloss, C., Wagner, V., Henderson, A. P., Golding, B. T., Wirtz, K., Martin-Reviejo, M., and Pilling, M. J.: Measurments of photo-oxidation products from the reaction of a series of alkyl-benzenes with hydroxyl radicals during EXACT using comprehensive gas chromatography, Atmos. Chem. Phys., 3, 1999–2014, 2003, http://www.atmos-chem-phys.net/3/1999/2003/.
Hansel, A., and Wisthaler, A.: A Method for Real-Time Detection of PAN, PPN and MPAN in Ambient Air, Geophys. Res. Lett., 27(6), 895–898, 2000.
Havers, N., Burba, P., Lambert, J., and Klockow, D.: Spectroscopic Characterization of HumicLike Substances in Airborne Particulate Matter, J. Atmos. Chem., 29, 45–54, 1998.
Holmes, N. S.: A review of particle formation events and growth in the atmosphere in the various environments and discussion of mechanistic implications, Atmos. Environ., 41, 2183–2201, 2007.
IPCC: Intergovernmental Panel on Climate Change, Fourth Assessment Report, Climate Change, 2007.
Izumi, K., Murano, K., Mizuochi, M., and Fukuyama, T.: Aerosol Formation by the Photooxidation of Cyclohexene in the Presence of Nitrogen Oxides, Environ. Sci. Technol., 22, 1207-1215, 1988.
Jang, M., and Kamens, R. M.: Atmospheric Secondary Aerosol Formation by Heterogeneous Reactions of Aldehydes in the Presence of a Sulfuric Acid Aerosol Catalyst, Environ. Sci.

Technol., 35, 4758–4766, 2001.
Jang, M., Lee, S., and Kamens, R. M.: Organic aerosol growth by acid-catalyzed heterogeneous reactions of octanal in a flow reactor, Atmos. Environ., 37(15), 2125–2138, 2003.
Jenkin, M. E., Saunders, S. M., Wagner, V., and Pilling, M. J.: Protocol for the development of the Master Chemical Mechanism MCM v3 (Part B): tropospheric degredation of aromatic volatile organic compounds, Atmos. Chem. Phys., 3, 181–193, 2003, http://www.atmos-chem-phys.net/3/181/2003/.
Johnson, D., Jenkin, M. E., Wirtz, K., and Martin-Reviejo, M.: Simulating the Formation of Secondary Organic Aerosol from the Photooxidation of Toluene, Environ. Chem., 1, 150–165, 2004.
Johnson, D., Jenkin, M. E., Wirtz, K., and Martin-Reviejo, M.: Simulating the Formation of Secondary Organic Aerosol from the Photooxidation of Aromatic Hydrocarbons, Environ. Chem., 2, 35–48, 2005.
Kalberer, M., Paulsen, D., Sax, M., Steinbacher, M., Dommen, J., Prevot, A. S. H., Fisseha, R., Weingartner, E., Frankevich, V., Zenobi, R., and Baltensperger, U.: Identification of polymers as major components of atmospheric organic aerosols, Science, 303(1659), 1659–1662, 2004.
Kalberer, M., Sax, M., and Samburova, V.: Molecular Size Evolution of Oligomers in Organic Aerosols Collectes in Urban Atmospheres and Generated in a Smog Chamber, Environ. Sci. Technol., 40, 5917–5922, 2006.
Kanakidou, M., Seinfeld, J. H., Pandis, S. N., Barnes, I., Detener, F. J., Facchini, M. C., Van Dingenen, R., Ervens, B., Nenes, A., Nielsen, C. J., Swietlicki, E., Putaud, J. P., Balkanski, Y., Fuzzi, S., Horth, J., Moortgat, G. K., Winterhalter, R., Myhre, C. L., Tsigaridis, K., Vignati, E., Stephanou, E. G., and Wilson, J.: Organic aerosol and global climate modelling: a review, Atmos. Chem. Phys., 5, 1053–1123, 2005, http://www.atmos-chem-phys.net/5/1053/2005/.
Kleindienst, T. E., Edney, E. O., Lewandowski, M., Offenberg, J. H., and Jaoui, M.: Secondary Organic Carbon and Aerosol Yields from the Irradiations of Isoprene and r-Pinene in the Presence of NOx and SO2, Environ. Sci. Technol., 40(12), 3807–3812, 2006.
Kleindienst, T. E., Smith, D. F., Li, W., Edney, E. O., Driscoll, D. J., Speer, R. E., and Weathers, W. S.: Secondary organic aerosol formation from the oxidation of aromatic hydrocarbon in the presence of dry submicron ammonium sulfate aerosol, Atmos. Environ., 33, 3669–3681, 1999.

Limbeck, A., Kulmala, M., and Puxbaum, H.: Secondary organic aerosol formation in the atmosphere via heterogeneous reaction of gaseous isoprene on acid particles, Geophys. Res. Lett., 30(19), 1996, doi:10.1029/2003GL017738, 2003.

Lindinger, W., Hirber, J., and Paretzke, H.: An ion/molecule-reaction mass spectrometer used for on-line trace gas analysis, International Journal of Mass Spectrometry and Ion Processes, 129, 79–88, 1993.

Monks, P. S.: Gas-phase radical chemistry in the troposphere, Chem. Soc. Rev., 34(5), 376–395, 2005.

Monks, P. S., Carpenter, L. J., Penkett, S. A., Ayers, G. P., Gillett, R. W., Galbally, I. E., and Meyer, C. P.: Fundamental ozone photochemistry in the remote marine boundary layer: The SOAPEX experiment, measurement and theory, Atmos. Environ., 32(21), 3647–3664, 1998.

Ng, N. L., Kroll, J. H., Chan, A. W. H., Chhabra, P. S., Flagan, R. C., and Seinfeld, J. H.: Secondary Organic Aerosol Fromation from *m*-xylene, toluene, and benzene, Atmos. Chem. Phys., 7, 4085–4126, 2007, http://www.atmos-chem-phys.net/7/4085/2007/.

Ng, N. L., Kroll, J. H., Keywood, M., Bahreini, R., Varutbangkul, V., Flagan, R. C., and Seinfeld, J. H.: Contribution of First- versus Second-Generation Products to Secondary Organic Aerosols Formed in the Oxidation of Biogenic Hydrocarbons, Environ. Sci. Technol., 40, 2283–2297, 2006.

Northcross, A. L., and Jang, M.: Heterogeneous SOA yield from ozonolysis of monoterpenes in the presence of inorganic acid, Atmos. Environ., 41(7), 1483–1493, 2007.

Odum, J. R.,Hoffman, T., Bowman, F., Collins, D., Flagan, R. C., and Seinfeld, J. H.: Gas/Particle Partitioning and Secondary Organic Aerosol Yields, Environ. Sci. Technol., 30, 2580–2585, 1996.

Odum, J. R., Jungkamp, T. P. W., Griffin, R. J., Flagan, R. C., and Seinfeld, J. H.: The Atmospheric Aerosol-Formation Potential of Whole Gasoline Vapor, Science, 276, 96–99, 1997.

Parker, A. E. Measurements of Peroxy Radicals Chemistry and Transport in the Atmosphere. Ph.D Thesis, Department of Chemistry, Leicester, University of Leicester, 2007.

Paulsen, D., Dommen, J., Kalberer, M., Prevot, A. S. H., Richter, R., Sax, M., Steinbacher, M., Weingartner, E., and Baltensperger, U.: Secondary organic aerosol formation by irradiation of 1,3,5-trimethylbenzene-NOx-H2O in a new reaction chamber for atmospheric chemistry and physics, Environ. Sci. Technol., 39(8), 2668–2678, 2005.

Sax, M., Zenobi, R., Baltensperger, U., and Kalberer, M.: Time Resolved Infrared Spectro-

scopic Analysis of Aerosol Formed by Photooxidation of 1,3,5-Trimethylbenzene and α-Pinene, Aerosol Science and Technology, 39, 822–830, 2005.

Seinfeld, J. H., and Pankow, J. F.: Organic Atmospheric Particulate Material, Annual Review of Physical Chemistry, 54, 121–140, 2003.

Smith, D. F., Kleindienst, T. E., and McIver, C. D.: Primary Production Distributions from the Reactions of OH with m-,p-Xylene, 1,2,4- and 1,3,5-Trimethylbenzene, J. Atmos. Chem., 34, 339–364, 1999.

Song, C., Kwangsam, N., and Cocker, D. R.: Impact of the Hydrocarbon to NOx Ratio on Secondary Organic Aerosol Formation, Environ. Sci. Technol., 39, 3143–3149, 2005.

Stern, J. E., Flagan, R. C., Grosjean, D., and Seinfeld, J. H.: Aerosol Formation and Growth in Atmospheric Aromatic Hydrocarbon Oxidation, Environ. Sci. Technol., 21(12), 1224–1231, 1987.

Stroud, C. A., Makar, P. A., Michelangeli, D. V., Mozurkewich, M., Hastie, D. R., Barbu, A., and Humble, J.: Simulating Organic Aerosol Formation during the Photoxidation of Toluene/NOx Mixtures: Comparing the Equilibrium and Kinetic Assumptions, Environ. Sci. Technol., 38, 1471–1479, 2004.

Surratt, J. D., Lewandowski, M., Offenberg, J. H., Jaoui, M., Kleindienst, T. E., Edney, E. O., and Seinfeld, J. H.: Effect of acidity on secondary organic aerosol formation from isoprene, Environ. Sci. Technol., 41(15), 5363–5369, 2007.

Surratt, J. D., Murphy, S. M., Kroll, J. H., Ng, N. L., Hilderbrandt, L., Sorooshian, A., Szmigielski, R., Vermeylen, R., Maenhaut, W., Claeys, M., Flagen, R., and Seinfeld, J. H.: Chemical Composition of Secondary Organic Aerosol Formed from the Photooxidation of Isoprene, J. Phys. Chem. A, 110, 9665–9690, 2006.

Taira, M., and Yukio, K.: Continuous Generation System for Low-Concentration Gaseous Nitrous Acid, Analytical Chemistry, 62, 630–633, 1990.

Tolocka, M. P., Jang, M., Ginter, J. M., Cox, F. J., Kamens, R. M., and Johnston, M. V.: Formation of Oligomers in Secondary Organic Aerosol, Environ. Sci. Technol., 38, 1428–1434, 2004.

Tsigaridis, K., and Kanakidou, M.: Global modelling of secondary organic aerosol in the troposphere: A sensitivity analysis, Atmos. Chem. Phys. Discuss., 3, 2879–2929, 2003, http://www.atmos-chem-phys-discuss.net/3/2879/2003/.

Verheggen, B., Mozurkewich, M., Caffrey, P., Frick, G., Hoppel, W., and Sullivan, W.: alpha-Pinene oxidation in the presence of seed aerosol: Estimates of nucleation rates, growth

rates, and yield, Environ. Sci. Technol., 41(17), 6046–6051, 2007.
Wyche, K. P., Blake, R. S., Ellis, A. M., Monks, P. S., Brauers, T., Koppman, R., and Apel, E.: Performance of a Chemical Ionisation Reaction Time-of-Flight Mass Spectrometer (CIR-TOF-MS) for the Measurement of Atmospherically Significant Oxygenated Volatile Organic Compounds, Atmos. Chem. Phys.,7, 609–620, 2007.
Yu, J., Jeffries, H. E., and Sexton, K. G.: Atmospheric Photooxidation of Alkylbenzenes-I. Carbonyl Product Analysis, Atmos. Environ., 31(15), 2261–2280, 1997.

Table 1. Summary of the major gas phase parameters for Experiments 1–7 along with CIR-TOF-MS conditions applied for VOC monitoring.

Exp. No.	Initial [VOC]/ ppbV	Initial [NO]/ ppbV	Initial [NO_b]/ ppbV	VOC/NO_x Ratio	Relative Humidity/ %	Exp. Duration[a]/ Mins.	Estimated [OH][b]/ pptV	CIR-MS Conditions[c] (E/N)/Td
1	560	129	141	2.07	52	539	0.04	120/170
2	1.180	535	0	2.21	49	521	0.02	120/170
3	143	134	129	0.54	48	596	0.06	140/140
4	554	135	129	2.10	52	521	0.02	120/150
5	151	Continuous HONO input[d]		∼15.10	62	488	0.05	90/150
6	597	135	130	2.25	53	462	0.03	90/190
7	166	Continuous HONO input[d]		∼16.60	50	549	0.06	90/190

[a] Experiment duration taken from the time that chamber lights were switched on.
[b] Estimated average [OH] over the entire Experiment.
[c] E/N conditions of the centre reaction cell/CDC ramping region.
[d] HONO injected continuously throughout experiment, chamber concentration ∼10 ppbV.

Table 2. Summary of the aerosol phase parameter for experiments 1–7.

Exp. No.	CPC Nuc. T[a] /Mins.	SMPS Nuc. T[b] /Mins.	[No.] Half Max. /Mins.	Max. [No.][c] /#cm-3	Time Max. [No.] /Mins.	[NO][c] Nucleation/ ppbV	[NO]→0 Time[d] /Mins.	Aerosol Diameter (Time) /nm (Mins.)	Aerosol Mass (Time) /μg m^{-3} (Mins.)	SOA Yield /%
1	108	108	183	580	225	16.2	152	387 (357)	47 (465)	1.94
2	145	149	167	1099	228	6.2	152–169[e]	663 (505)	182 (433)	7.47
3	400	420	543	406	609	1.4	325	155 (618)	2 (621)	0.29
4	188	193	226	491	256	1.2	157	507 (484)	36 (415)	2.29
5	50	58	94	407	163	0.4	–[f]	462 (513)	33 (504)	7.87
6	184	182	218	494	257	1.4	162	484 (487)	31 (358)	1.79
7	22	28	43	2216	76	0.4	–[f]	404 (550)	45 (487)	6.21

[a] Nucleation time obtained using data from CPC (particles of diameter ≥3 nm).
[b] Nucleation time obtained using data from SMPS (particles of diameter ≥15 nm).
[c] Data obtained from SMPS.
[d] Defined as the time at which [NO] reaches 2 ppbV.
[e] NO analyser off line, [NO] dropped below 2 ppbV during this time.
[f] Low NO_x experiment, [NO] <1 ppbV throughout Experiment.

Table 3. Key TMB, O_3 and NO_2 parameters for Experiments 1–7.

Exp. No.	HC Consumed/ %	Peak d[TMB]/dt /Mins.	Peak [O_3] Time /Mins.	Peak [O_3] /ppbV	Peak [NO_2] Time/Mins.	Peak [NO_2] /ppbV
1	89.4	130	278	274.1	103	212.7
2	44.3	120	259	365.2	137	446.2
3	91.5	120	600	199.1	188	187.4
4	63.5	110	287	230.8	104	196.4
5	82.2	–	489	43.8	–	–
6	62.1	110	284	226.3	110	200.9
7	92.5	–	551	58.9	–	–

Table 4. Most major VOC contributors to the gas phase as measured by CIR-TOF-MS. Measured m/z, approximate peak signal intensity, appearance time and tentative assignments are included. MCM species names are included and can be used for navigation around the MCMv3.1 TMB degradation scheme via the MCM website (http://mcm.leeds.ac.uk/MCM).

				Appearance Time/Minutes						
Measured m/z	Peak Signal/ncps	Tentative Assignment Name (MCM designation)/(Fig. 6 identifier)	Mass/Da	Exp 1	Exp 2	Exp 3	Exp 4	Exp 5	Exp 6	Exp 7
232.20	200	1,3,5-Trimethyl-4-nitrooxy-6,7-dioxa-bicyclo[3.2.1]oct-2-en-8-ol (TM135BPNO3)/(L)	231.20	120	90	n/m	51	36	51	3
214.15	200	TM135BPNO3 Fragment: $MH^+[-H_2O]$	213.19	96	100	87	81	33	12	27
185.20	300	8-Hydroxy-1,3,5-trimethyl-6,7-dioxa-bicyclo[3.2.1]oct-3-en-2-one (TM135OBPOH)/(P)	184.19	130	130	288*	108	24	60	15
		2-Methyl-3-(1-methyl-3-oxo-but-1-enyl)-oxirane-2-carboxylic acid (TM135MUO2H)	184.19							
169.22	70	1,3,5-Trimethyl-6,7-dioxa-bicyclo[3.2.1]oct-3-ene-2,8-diol (TM135BP2OH)/(O) Fragment: $MH^+[-H_2O]$	169.20	36	93	n/m	69	36	42	3
		2-Methyl-3-(1-methyl-3-oxo-but-1-enyl)-oxirane-2-carbaldehyde (TM135OXMUC)	168.19							
167.18	120	3,5-Dimethyl-benzenecarboperoxoic acid (TMBCO3H)	166.18	147	177	n/m	81	114	63	n/m
157.20	150	5-Hydroxy-4-methyl-hept-3-ene-2,6-dione (C7M2CO5OH)	156.18	150	126	240	99	102	66	24
155.18	120	4-Methyl-hept-4-ene-2,3,6-trione (C7M3CO)	154.17	453*	171	n/m	111	183	129	30*

n/a = Mass not applicable
n/m = Compound not measured during specific Experiment
* = Weak signal, appearance time not reported

Table 4. Continued.

				Appearance Time/Minutes						
Measured m/z	Peak Signal/ncps	Tentative Assignment Name (MCM designation)/(Fig. 6 identifier)	Mass/Da	Exp 1	Exp 2	Exp 3	Exp 4	Exp 5	Exp 6	Exp 7
153.22	100	(3,5-Dimethyl-phenyl)-methyl-hydroperoxide (TM-BOOH)	152.20							
151.17	160	3,5-dimethylbenzoic acid (TMBCO2H)	150.18	105	84	465*	72	135	60	39*
		2-Methyl-4-oxo-pent-2-enoic acid (C5CODBCO3H)	144.13							
145.17	50	2-Hydroxy-2-methyl-3,4-dioxo-pentanal (C6CO3MOH)	144.13							
		2-Oxo-propionic acid 1-methyl-2-oxo-ethyl ester (C23O3MCHO)	144.13							
		1-(3-Methyl-3-vinyl-oxiranyl)-ethanone (EPXMALKT)	144.13							
143.19	120	Unidentified	n/a	366*	*	406*	129	78	75	30*
141.18	140	Unidentified	n/a	126	111	*	132	138	75	60
139.18	400	3,5-Dimethyl-phenyl-hydroperoxide (DMPHOOH)	138.16	309*	78	*	51	3	66	3
137.19	220	2,4,6-trimethyl phenol (TM135BZOL)/(D)	136.19	81	75	96	54	*	15	15
		(3,5-Dimethyl-phenyl)-methanol (TMBOH)	136.19							
		m-xyloquinone	136.15							
136.09	400	Unidentified nitrate	n/a	114	132	141	87	45	96	n/m
		3,5-dimethyl benzaldehyde (TMBCHO)/(W)	134.18							
135.18	1000	2-Hydroxy-2-methyl-3-oxo-propaneperoxoic acid (CHOMOHCO3H)	134.09	63	78	93	57	30	39	18

Table 4. Continued.

				Appearance Time/Minutes						
Measured m/z	Peak Signal/ncps	Tentative Assignment Name (MCM designation)/(Fig. 6 identifier)	Mass/Da	Exp 1	Exp 2	Exp 3	Exp 4	Exp 5	Exp 6	Exp 7
		2-Hydroxy-3-oxo-butaneperoxoic acid (CO2H3CO3H)	134.09							
		Malic acid	134.09							
129.17	500	2-Methyl-4-oxo-pent-2-enoic acid (C5CODBCO2H)	128.12	84	93	168	66	3	72	33
		3-Acetyl-2-methyl-oxirane-2-carbaldehyde (EXPMALKT)	128.12							
127.17	300	Related to Bicyclic Signals	n/a	90	90	144	96	99	57	27
125.15	1200	Bicyclic Fragment: $[C_6H_3O_3]H^+$	125.10	99	102	69	45	3	33	3
123.17	400	Unidentified	*	*	*	183*	*	*	*	*
119.18	200	2-Hydroperoxy-2-methyl-malonaldehyde (C3MDIALOOH)	118.09	90	75	*	123	33	69	3*
		Succinic acid	118.09							
117.14	140	3-Hydroxy-pentane-2,4-dione (C5CO243OH)	116.12	174	129	183	84	42	81	12
115.13	250	Pentane-2,3,4-trione (C5CO234)	114.10	153	108	183	111	18	3	33*
		Methyl maleic anhydride (MMALANHY)/(AF)	112.08							
113.13	7400			15	15	33	15	9	3	6
		2-methyl-4-oxo-2-pentenal (C5MDICARB)/(R)	112.13							
		3,5-dimethyl-3(2H)-2-furanone/(AF)	112.13							
		3,5-dimethyl-5(2H)-2-furanone (MXFUONE)/(S)	112.13							

Table 4. Continued.

				Appearance Time/Minutes						
Measured m/z	Peak Signal/ncps	Tentative Assignment Name (MCM designation)/(Fig. 6 identifier)	Mass/Da	Exp 1	2	Exp 3	Exp 4	Exp 5	Exp 6	Exp 7
111.12	6000	3 methyl-5-methylidene-5-(2H) furanone	110.04	72	60	105	66	15	21	39
109.15	400	TM135BPNO3 Fragment: MH^+[– $O.NO_3.3(CH_3)$]	109.10	84	75	51	60	3	54	3
103.11	150	2-Hydroxy-2-methyl-malonaldehyde (C3MDIALOH)	102.09	150	126	*	126	93	12	27
101.13	400	2,3-dioxobutanal	100.7	126	90	129	84	60	12	15
99.12	160	Unidentified	n/a	183	171	n/m	177*	366	99	30*
97.13	1000	Unidentified	n/a	72	78	102	81	51	9	33
87.10	1200	Related to Bicyclic Signals	n/a	117	75	123	90	42	12	24
85.11	500	m/z 113 Fragment: MH^+[-CO] Butenedial	85.13 84.07	84	63	81	51	63	33	27
77.07	1400	Hydroxy acetic acid (CH3CO3H)	76.05	99	135	168	90	36	63	15
75.09	400	Hydroxyacetone	74.08	141	66	147	105	72	66	3
		Oxo-acetic acid (HCOCO2H)	74.04							
73.07	1600	Methyl glyoxal (MGLYOX)/(Q)	72.06	36	30	39	15	9	36	15
		Acetic Acid (CH3CO2H)/(X)	60.05							
61.07	6000	Glycoaldehyde	60.50	36	72	60	90	12	18	3
		Pyruvic Acid Fragment	88.06							
		Lactic Acid Fragment	90.08							

Table 4. Continued.

				Appearance Time/Minutes						
Measured m/z	Peak Signal/ncps	Tentative Assignment Name (MCM designation)/(Fig. 6 identifier)	Mass/Da	Exp 1	Exp 2	Exp 3	Exp 4	Exp 5	Exp 6	Exp 7
59.08	1200	Acetone	58.08	n/m	n/m	174	51	72*	207	27
57.10	1000	Carbonyl/Hydrocarbon Fragment: $[C_3H_5O^+]$ / $[C_4H_9^+]$	57.07 / 57.12	225	141	n/m	147	114	183	51
47.01	600	Formic Acid/(Y)	46.03	198	105	69	72	72	252	*
46.01	5000	PAN Fragment: $[NO_2^+]$	46.01	102	105	105	72	93	72	51
45.06	3500	Me. Glyoxal Fragment (CH3OOH)/(AD)	44.05	63	42	93	48	99	45	12
43.04	5000	Carbonyl/Hydrocarbon Fragment: $[C_2H_3O^+]$ / $[C_3H_7^+]$	43.05 / 43.09	63	18	69	57	3	3	0
33.05	5000	Methanol (CH3OH)/(AA)	32.04	105	141	399*	106	132	153	90
31.03	1000	Formaldehyde (HCHO)/(AB)	30.03	264	159	345*	132*	243*	249	27

Table A1. CIR-TOF-MS calibration details. The measured compound is given along with the method employed for calibration, the relative humidity of the sample matrix during calibration and, where appropriate the surrogate compound employed. The instrument sensitivity to each given compound is provided along with an uncertainty/error estimate for the measurement.

Target	Method	Relative Humidity/%	Calibration Compound	Sensitivity[a]/ncps ppbV^{-1}	Calibration Error[b]/%
2,4,6-trimethyl phenol	Gas Standard[c]	0	Phenol	226.35–372.54	11.04–21.78
3,5-dimethyl benzaldehyde	Gas Standard	0	m-tolualdehyde	98.65–145.35	9.35–17.20
O_2 Bridged Nitrate (TM135BPNO3)[d]	Gas Standard	0	m-tolualdehyde	98.65–145.35	9.35–17.20
O_2 Bridged Diol (TM135BP2OH)[d]	Gas Standard	0	m-tolualdehyde	98.65–145.35	9.35–17.20
O_2 Bridged Ketone (TM135OBPOH)[d]	Gas Standard	0	m-tolualdehyde	98.65–145.35	9.35–17.20
Bicyclic Marker[d]	Gas Standard	0	m-tolualdehyde	98.65–145.35	9.35–17.20
m/z 129	Permeation Tube	50	Methacrolein	9.46–19.27	3.95–4.20
Unsaturated Anhydrides (m/z 111 & 113)	Teflon Bag[e]	50	Citraconic Anhydride	32.53–119.90	27.60–27.63
Hydroxy Acetic Acid	Permeation Tube[f]	50	Acetic Acid	17.43–45.93	2.93–5.96
Hydroxy Acetone	Permeation Tube	50	Acetone	55.60–104.04	3.25–4.87
Methyl Glyoxal	Permeation Tube	50	Isoprene	9.46–19.27	6.53–11.56
Acetic Acid	Permeation Tube	50	Acetic Acid	17.43–45.93	2.93–5.96
Acetone	Permeation Tube	50	Acetone	55.60–104.04	3.25–4.87
Formic Acid	Permeation Tube	50	Formic Acid	5.14–9.52	3.77–6.78
Acetaldehyde	Permeation Tube	50	Acetaldehyde	57.01–107.33	3.17–3.31
Carbonyl Marker	Permeation Tube	50	Acetone	55.60–104.04	3.25–4.87
Methanol	Permeation Tube	50	Methanol	22.25–46.06	3/94–6.76

[a] Instrument sensitivity is given as a range covering all drift cell conditions employed during the study (see Table 1 for further information).
[b] Measurement uncertainty/error is given as a range covering all drift cell conditions employed during the study (see Table 1 for further information).
[c] Gas standards provided by Air Environmental Inc. (US) and courtesy of PSI. Compound mixing ratio accuracy: 10%.
[d] Calibrated values used only to calculate "pseudo" VOC yields.
[e] Calibration conducted by injecting liquid citraconic anhydride (Sigma Aldrich, 99%) into an 80 L Teflon sample bag (SKC, Ltd). Sticking factors employed to adjust for deposition/wall loss.
[f] Permeation tubes supplied by Ecoscientific (UK) and Vici Inc. (US). Compound emission rate accuracy: 2.02–11.24%.

Table A2. VOC yields for various compounds measured by CIR-TOF-MS during Experiments 1–7.

	Volatile Organic Compound Product Yield / %						
Experiment	1	2	3	4	5	6	7
Compound							
O_2 Bridged Nitrate (TM135BPNO3)	1.8	2.8	2.7	2.9	4.3	3.7	5.1
O_2 Bridged Ketone (TM135OBPOH)	0.7	0.6	1.0	1.1	3.0	0.8	2.3
O_2 Bridged Diol (TM13BP2OH)	0.2	0.3	n/m	0.4	0.8	0.2	0.9
3,5-dimethylphenol							
3,5-dimethyl benzaldehyde	1.3	2.5	1.6	2.6	1.9	2.7	2.2
m/z 129	5.0	4.4	11.8	18.6	29.5	8.4	12.9
m/z 113	15.6	46.6	37.2	38.4	33.3	39.6	26.5
3 Me. 5-methyl-5-(2H) furanone	5.7	10.3	8.8	7.9	3.6	8.1	8.9
Hydroxy-acetone	0.6	0.5	1.1	1.0	1.5	0.6	1.2
Hydroxy acetic acid	3.1	n/m	2.0	3.1	18.6	5.9	8.3
Methyl glyoxal	13.5	24.3	31.1	28.8	21.3	22.5	21.0
Acetic acid	19.5	14.7	11.9	10.0	33.1	16.0	32.2
Acetone	n/m	0.4	3.3	1.4	3.1	1.3	1.5
Formic acid	11.51	13.1	32.5	15.3	48.5	10.9	n/m
Carbonyls	32.1	44.7	51.2	26.2	17.8	24.9	41.2
Methanol	1.7	1.0	1.0	0.7	2.8	1.4	2.6

n/m: Not measured

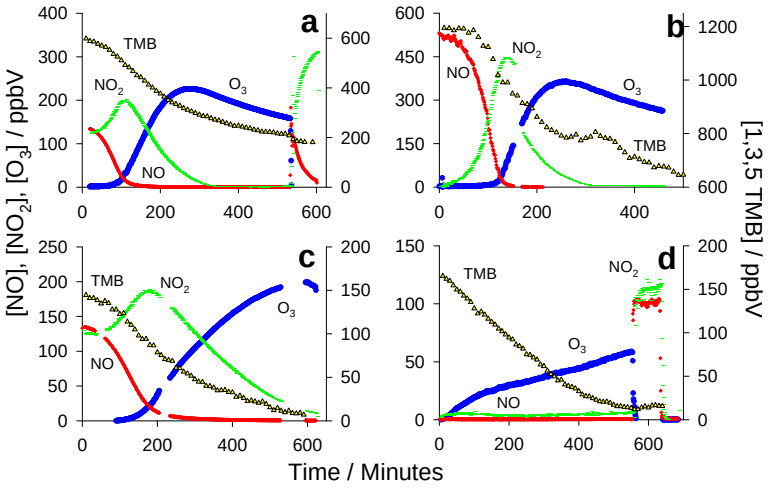

Fig. 1. Temporal evolution of the major gas phase components of the 1,3,5-TMB photooxidation system during **(a)** Experiment 6 (VOC/NO_x~2:1), **(b)** Experiment 2 (VOC/NO_x~2:1, NO only), **(c)** Experiment 3 (VOC/NO_x~1:2) and **(d)** Experiment 7 (VOC/NO_x~17:1). In each plot the left ordinate axis gives the concentration of the inorganic components (NO, NO_2 and O_3) while the right axis gives the concentration of TMB.

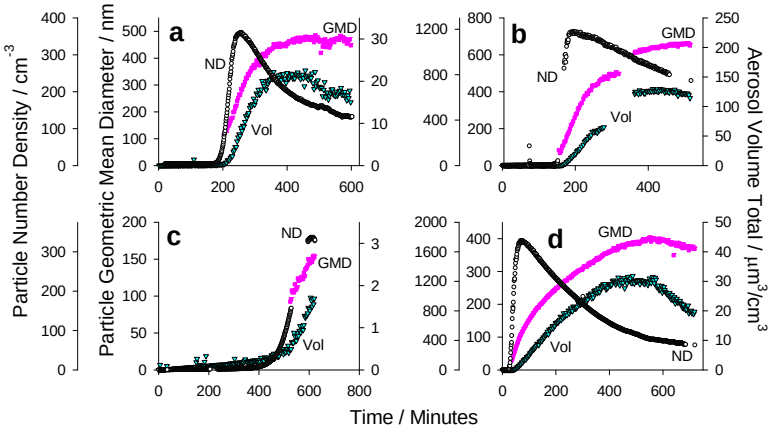

Fig. 2. Temporal evolution of the aerosol number density (ND), geometric mean diameter (GMD) and volume concentration (Vol) within the chamber during **(a)** Experiment 6 (VOC/NO_x~2:1), **(b)** Experiment 2 (VOC/NO_x~2:1, NO only), **(c)** Experiment 3 (VOC/NO_x~1:2) and **(d)** Experiment 7 (VOC/NO_x~17:1).

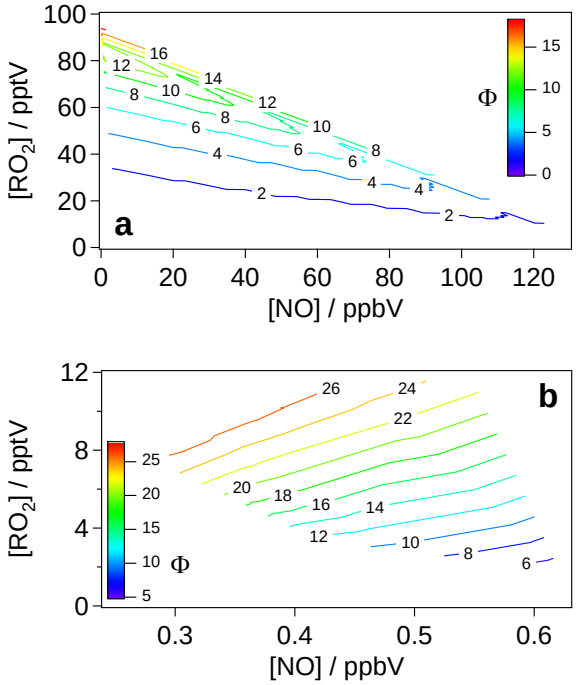

Fig. 3. Theoretical variation in partitioning of RO_2 species with evolving chamber [NO] for **(a)** high NO_x conditions and **(b)** low NO_x conditions. Φ gives the percentage of RO_2 species forming peroxides (see Eq. 2 and text for further details).

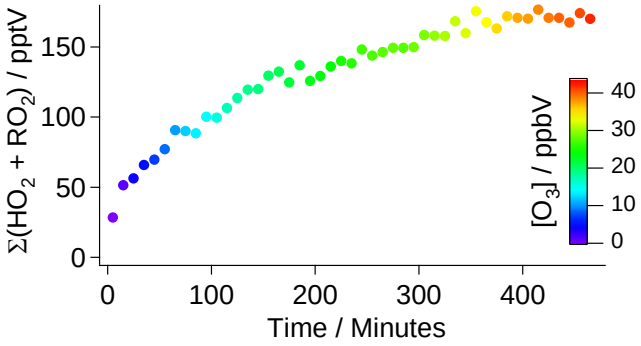

Fig. 4. Temporal evolution of the sum of hydro and organic peroxy radicals (i.e. $\sum(HO_2+RO_2)$) recorded by the PERCA during the low NO_x Experiment 5 (VOC/NO_x ratio ~15:1).

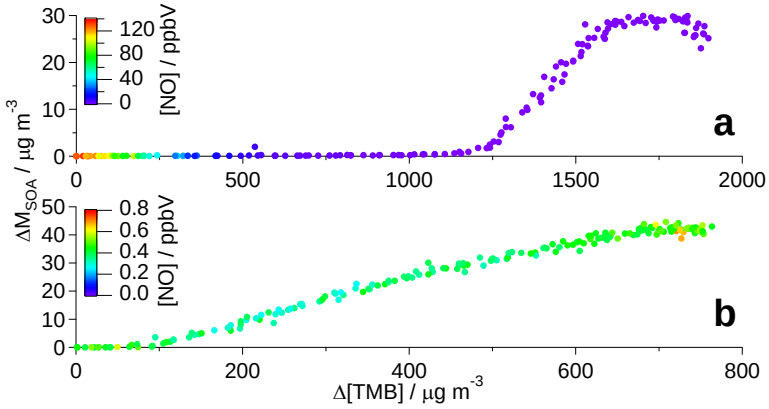

Fig. 5. SOA growth curves for **(a)** Experiment 6 (high NO_x experiment, VOC/NO_x~2:1) and **(b)** Experiment 7 (low NO_x experiment, VOC/NO_x~17:1). Δ[TMB]=reacted mass of TMB following initiation of the oxidation chemistry.

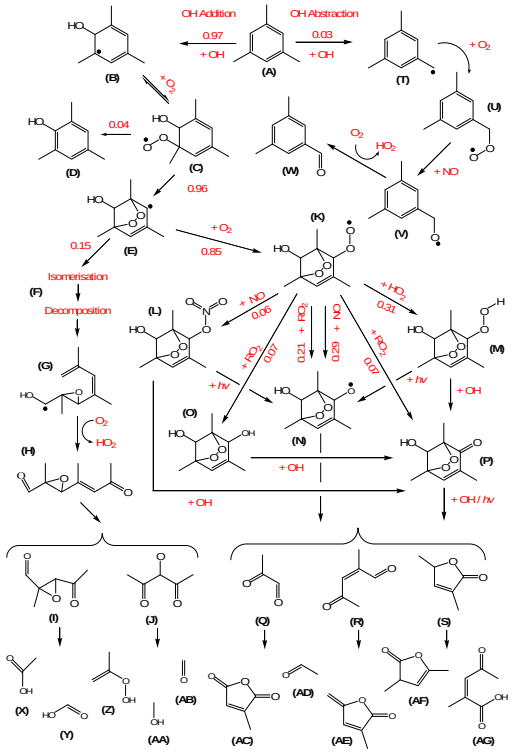

Fig. 6. Mechanism summary of OH radical-induced photooxidation of 1,3,5-trimethylbenzene. Key primary and secondary product formation shown, branching ratios are taken from MCMv3.1 (http://mcm.leeds.ac.uk/mcm) (see text).

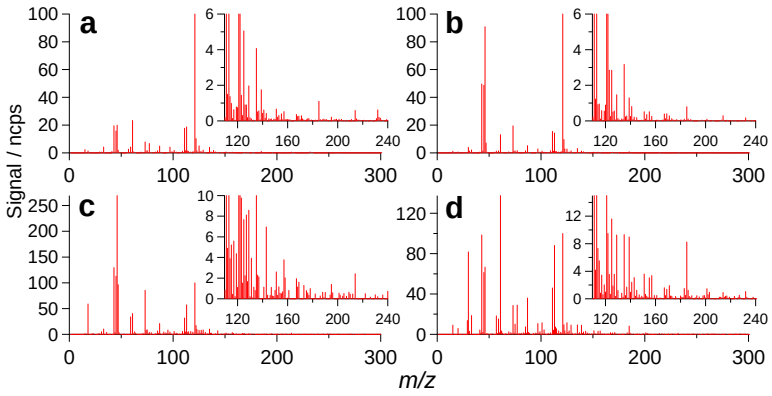

Fig. 7. Comparison of CIR-MS mass spectra recorded 400 minutes after the start of experiments for **(a)** Experiment 6 (VOC/NO_x~2:1), **(b)** Experiment 2 (VOC/NO_x~2:1, NO only), **(c)** Experiment 3 (VOC/NO_x~1:2) and **(d)** Experiment 7 (low NO_x, VOC/NO_x~17:1). Each mass spectrum corresponds to data accumulation for a ten-minute period.

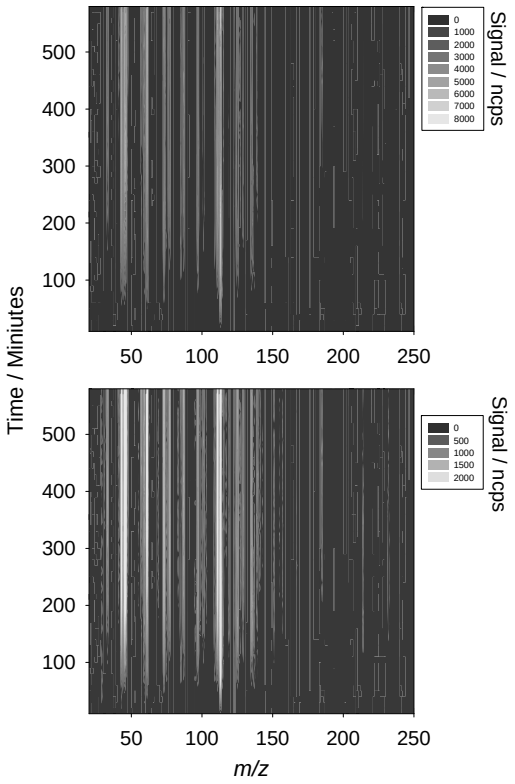

Fig. 8. Evolution of the gas phase organic species during Experiment 6 (VOC/NO_x~2:1).

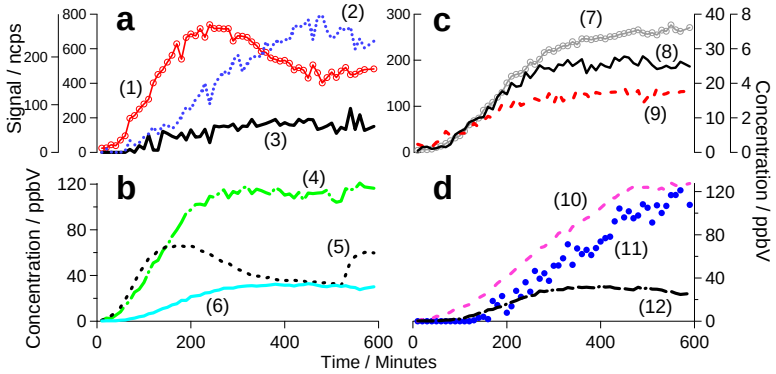

Fig. 9. Temporal evolution of certain key VOCs during the photooxidation of 1,3,5-TMB in Experiment 6 (VOC/NOx 2:1). **(a)** (1) O_2-bridged nitrate, (2) O_2-bridged ketone (on right axis), (3) O_2-bridged diol fragment, **(b)** (4) methyl glyoxal, (5) m/z 113-isobaric ring opening products citraconic anhydride, 3,5-dimethyl-3(2H)-2-furanone, 3,5- dimethyl-5(2H)-2-furanone and 2-methyl-4-oxo-2-pentenal,, (6) 3 methyl-5-methylidene-5-(2H)-furanone, **(c)** (7) m/z 43: carbonyl marker (left axis), (8) 2-methyl-4-oxo-pent-2-enoic acid and 3-acetyl- 2-methyl-oxirane-2-carbaldehyde (first right axis), (9) hydroxy acetone (second right axis) and **(d)** (10) acetic acid, (11) formic acid, (12) hydroxy acetic acid.

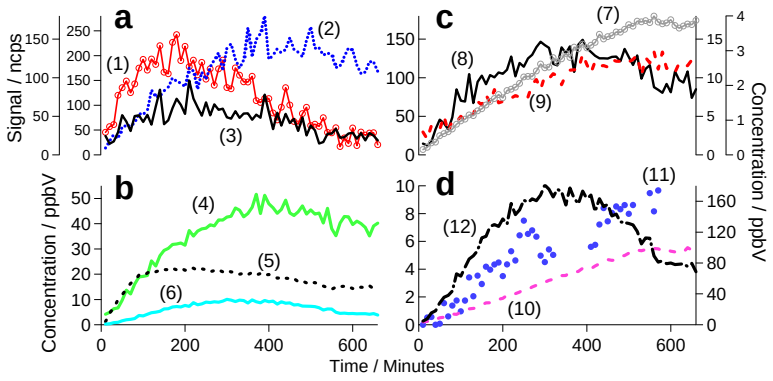

Fig. 10. Temporal evolution of certain key VOCs during the photooxidation of 1,3,5-TMB during experiment 7 (VOC/NO_x~17:1). Compound numbering is the same as that used in the caption for Fig. 9. Note: in figure **(a)** signal of O_2-bridged diol (3) is given on the right axis and in figure **(d)** concentration of hydroxyl acetic acid (10) is given on the left axis.

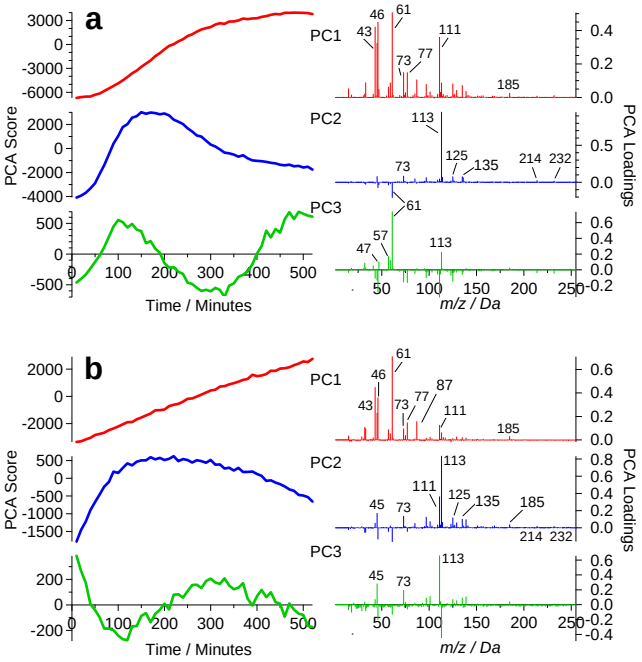

Fig. 11. Principal component analysis conducted on VOC data for **(a)** Experiment 6 (high NO_x, VOC/NO_x~2:1) and **(b)** Experiment 7 (low NO_x, VOC/NO_x~17:1). Percentage variance captured: PC1=78.0%, PC2=19.7% and PC3=1.9% for Experiment 6 and PC1=90.0%, PC2=8.0% and PC3=0.6% for Experiment 7.

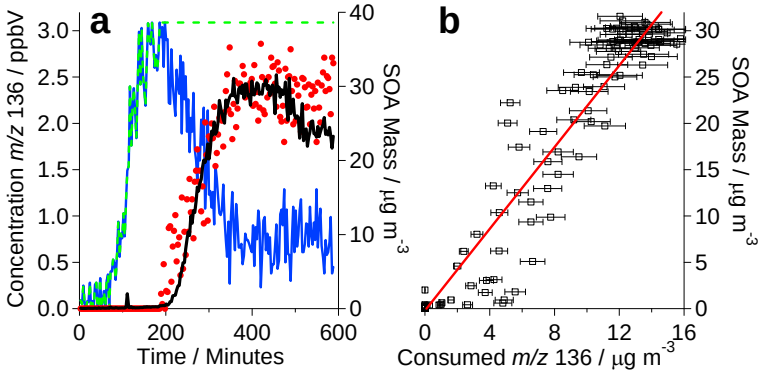

Fig. 12. **(a)** Temporal evolution of the unidentified nitrate of m/z 136 (solid blue line) during Experiment 6 (high NO_x). Plot includes total amount of m/z 136 formed (dashed green line) and total amount lost (red circles). Also included is an overlaid profile of SOA mass (solid black line). **(b)** Correlation between m/z 136 mass lost and SOA mass formed (up to the point of peak mass) for Experiment 6. Line fit: y=2.21 (±0.04)×−0.21 (±0.35), r^2=0.94. Coefficients quoted±one standard deviation.

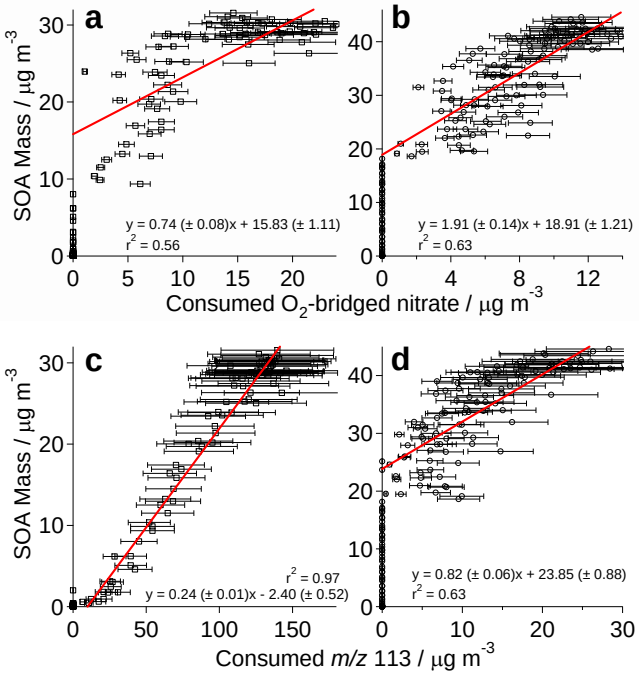

Fig. 13. Correlation between mass of VOC lost and mass of SOA formed (up to the point of peak mass), for the O_2-bridged nitrate for **(a)** Experiment 6 (high NO_x) and **(b)** Experiment 7 (low NO_x) and for the m/z 113 ring opening compounds for **(c)** Experiment 6 and **(d)** Experiment 7. Correlation coefficients quoted±one standard deviation.